Astron. Astrophys. 336, 697–720 (1998)

ASTRONOMY AND ASTROPHYSICS

On the fractal structure of molecular clouds

J. Stutzki, F. Bensch, A. Heithausen ⋆, V. Ossenkopf, and M. Zielinsky

Physikalisches Institut der Universität zu Köln, Zülpicher Strasse 77, D-50937 Köln, Germany (*lastname*@ph1.uni-koeln.de)

Received 5 January 1998 / Accepted 5 May 1998

Abstract. We present a new method to analyze the structure of observed molecular cloud images which is the generalization of the *Allan-variance* method traditionally used in the stability and drift analysis of instrumentation and electronic devices. Applied to integrated intensity maps of two molecular cloud data sets, the method shows, together with an analysis of the phases of the cloud images, the observed structures to be well characterized by what is called a *fractional Brownian motion (fBm)*-structure in the context of fractal images. An *fBm*-structure results from a power law power spectrum of the image and a completely random distribution of the image phases. The power law index β of the power spectrum derived for two sample clouds turns out to be close to 2.8. For an *fBm*-structure, the power spectral index β determines other fractal measures such as the traditionally used box-counting dimension and the fractal dimension describing iso-intensity contours via their area-perimeter relation. We use a large data set covering observations at both large and small angular scales available for the Polaris Flare (Heithausen et al. 1998) as the sample cloud to test these concepts. The area-perimeter dimension independently measured for this cloud is consistent with $\beta = 2.8$. The *fBm*-concept allows easy generation of realistic density representations for model clouds, to be used in radiative transfer and other cloud simulations.

In a second step, we show that an ensemble of randomly positioned clumps with a power law mass spectrum $dN/dM \propto M^{-\alpha}$ gives an *fBm*-image. The power spectral index β, the mass spectral index α, and the power law index of the mass-size relation $M \propto L^{\gamma}$ turn out to be related: $\beta = \gamma(3-\alpha)$. The value of γ derived via this relation and the independently determined values for α and β is consistent with the value directly determined for the sample cloud. Our analysis confirms the recent suggestion by Elmegreen & Falgarone (1996) that the mass distribution in molecular clouds is closely connected with their fractal structure, although the detailed form of the relation depends on the fractal structure model used.

We discuss the implications of these results, obtained for the 2-dimensional observed images, for the underlying 3-dimensional cloud density structure. With some extrapolating assumptions on the 3-dim structure, they imply that the 3-dimensional structure is very much broken up, with the surface growing proportional to the volume. Clearly, additional information on the velocity structure, and in particular its physical link to the assumed *fBm*-density structure, is needed to describe the relevant properties of molecular cloud line shapes and line radiative transfer.

The *fBm*-structure model allows an estimate on the observability of molecular cloud structure down to much smaller angular scales than presently reachable, e.g. with interferometric observations. It turns out that, due to the steepness of the image power spectrum, these will be extremely difficult. Only the next generation large mm-wave array will bring such observations into the regime of the feasible.

Key words: ISM: structure – ISM: clouds – ISM: general

1. Introduction

Observations of molecular clouds have shown that with each step in increasing spatial resolution we see the structure to break up into substructure down to the new resolution limit. This holds down to the highest linear resolution achievable (Langer et al. 1995, Falgarone & Phillips 1996). The presence of such clumpy structure has been inferred indirectly since early times of molecular cloud observations (see Stutzki (1993) for a review) from the small area filling factors of typically 10-20% (NH_3: Ho & Townes 1983; CS: Snell et al. 1984), or from the similarity of ^{12}CO and ^{13}CO line profiles despite of their large difference in optical depth (Martin et al. 1984).

The study of photo dissociation regions (PDRs) has given independent evidence for the clumpy structure of molecular clouds: only clumpiness with a clump-interclump density contrast of several factors of 10, allowing FUV penetration through the much less opaque interclump material much deeper into the cloud, can explain the large spatial extent and coexistence of several PDR tracers. (Stutzki et al. 1988; Howe et al. 1991). The low-J CO lines very commonly show line ratios in conflict with the emission originating in a homogeneous density and temperature structure: PDR models of UV illuminated clumps give a natural explanation of the observed line ratios over a large range of UV intensities and clump

Send offprint requests to: J. Stutzki

⋆ Present address: Radioastronomisches Institut der Universität Bonn, Auf dem Hügel 71, D-53121 Bonn, Germany

densities (Castets et al. 1990; Gierens et al. 1991; Köster et al. 1994; Störzer et al. 1996; and Störzer et al. 1997).

The observed line widths of molecular clouds are highly supra-thermal and the internal cloud motions would lead to very fast energy dissipation unless cushioned by coupled magnetic fields. Again, this scenario implies the presence of substructure, i.e. higher density clumps with intrinsically narrow lines moving around with a larger interclump velocity dispersion. The smoothness of the observed, close to Gaussian, line profiles at lower spatial resolution allows to infer a very large number of very small clumps (Tauber et al. 1991; Tauber 1996). Observations of the nearest molecular cloud L1457 (Zimmermann 1993) show that the line profiles indeed break up into many individual components at high spatial resolution.

Molecular cloud structure is obviously closely related to the star formation process, likely controlling the overall star formation efficiency and possibly the mass spectrum of the newly formed stars (Zinnecker 1989; Larson 1992). Also, the clumpy structure drastically enhances the back reaction of newly formed stars with the molecular material of their parent cloud, thus affecting the overall cloud evolution (Bertoldi & McKee 1996). The importance of molecular cloud structure has resulted in many attempts over the last few years to characterize the structure observed in a quantitative way, e.g. by means of autocorrelation analysis (Dickman & Kleiner 1985; Kleiner & Dickman 1987; Perault et al. 1986), measuring the area-perimeter relation for iso-intensity contours of 100 μm dust emission maps, dust extinction maps, and HI or CO integrated line intensity maps (Bazell & Desert 1988; Scalo 1990; Dickman et al. 1990; Falgarone et al. 1991; Zimmermann & Stutzki 1993; Vogelaar & Wakker 1994), wavelet analysis (Langer et al. 1993), structure tree methods (Houlahan & Scalo 1992) or by clump decomposition and the determination of clump mass spectra (Stutzki & Güsten 1990; Williams et al. 1994; Kramer et al. 1998). In a recent paper Elmegreen & Falgarone (1996) suggest that the mass distribution is the result of the fractal structure of the molecular cloud gas, and that the power law index of the clump mass spectrum and the fractal dimension of the cloud are thus related.

In this paper we investigate the structure of molecular cloud images, i.e. the spatial distribution of the line integrated intensity of a particular molecular transition used as a tracer for the molecular cloud material. In the optically thin limit and for uniform, thermalized excitation conditions the line integrated intensity basically measures the clouds column density, i.e. the 2-dimensional projection of the clouds density structure onto the plane of the sky. Obvious extensions of the present work, which will be presented in follow up papers, are for one to study the structure of individual velocity channel maps and the variation between those (Bensch et al., *in prep.*), and secondly to investigate the influence of optical depth effects on the structure of the observed integrated intensity image resulting from a given 3-dimensional density distribution (Ossenkopf et al., *in prep.*).

We discuss in Sect. 2 a new method for analyzing molecular cloud structure which is basically a 2-dimensional generalization of the *Allan variance* method used in the time stability analysis of sensitive equipment, e.g. atomic clocks (Allan 1966; Barnes et al. 1971) or radio astronomy receivers (Schieder et al. 1989). This analysis applied to observed molecular cloud images shows that the power spectrum of their images is a power law with the spectral index in a narrow range. Moreover, the phases in the Fourier-transformed image are distributed randomly. Molecular cloud structure thus may well be described as having a power law power spectrum and completely random phases, a structure that is called *fractional Brownian motion* structure in the theory of fractal images. In Sect. 3 we discuss the connection between the various methods commonly used for structure analysis of molecular clouds and show that they can be viewed in an unique way, connecting the various indices measured, like the fractal dimension from area-perimeter relations or from box coverage methods, power spectrum power law index or drift behavior. We show in Sect. 4 that artificial cloud images generated as *fractional Brownian motion* images give indeed a good simulation of real molecular cloud images. On this background, we derive in Sect. 5 that an ensemble of clumps with a given power law mass spectrum also gives a *fractional Brownian motion* image in its 2-dimensional projection, where the power spectrum spectral index is determined by the mass spectral index and the power law index in the mass-size relation of the clumps. In Sect. 6 we critically review the connection of the various fractal indices presented in the literature and derived in the present paper, with particular emphasis on the connection between the clump mass and size spectra, the mass-size relation and the fractal dimension of the cloud. The discussion in Sect. 7 addresses the implications of the observed structural parameters of the 2-dimensional observed cloud images for the intrinsic 3-dimensional cloud structure, the implications of the results for further observations down to yet higher angular resolution, and the limitation of the present analysis within the framework of more complex models for the cloud structure. The results are summarized in Sect. 8.

2. Power spectrum and phase distribution of molecular cloud images

Being generated predominantly by the turbulent internal cloud motion, the internal structure of molecular clouds is likely to be random to a large degree. All the information on the structural properties of a random function is contained in its *power spectrum*, the phase distribution being completely random. Thus, it is obviously important to study the *power spectrum* of observed cloud images. This has been done for HI clouds (Green 1993), deriving the azimuthally averaged *power spectra* directly from interferometer observations; he finds the *power spectra* to be smooth and well characterized by a power law with a spectral index around 2.6 to 2.8 for individual velocity channel maps.

2.1. The Δ-variance analysis: a generalized Allan-variance method

A very powerful tool to study the drift characteristics of a random time series has been introduced by Allan (1966), within

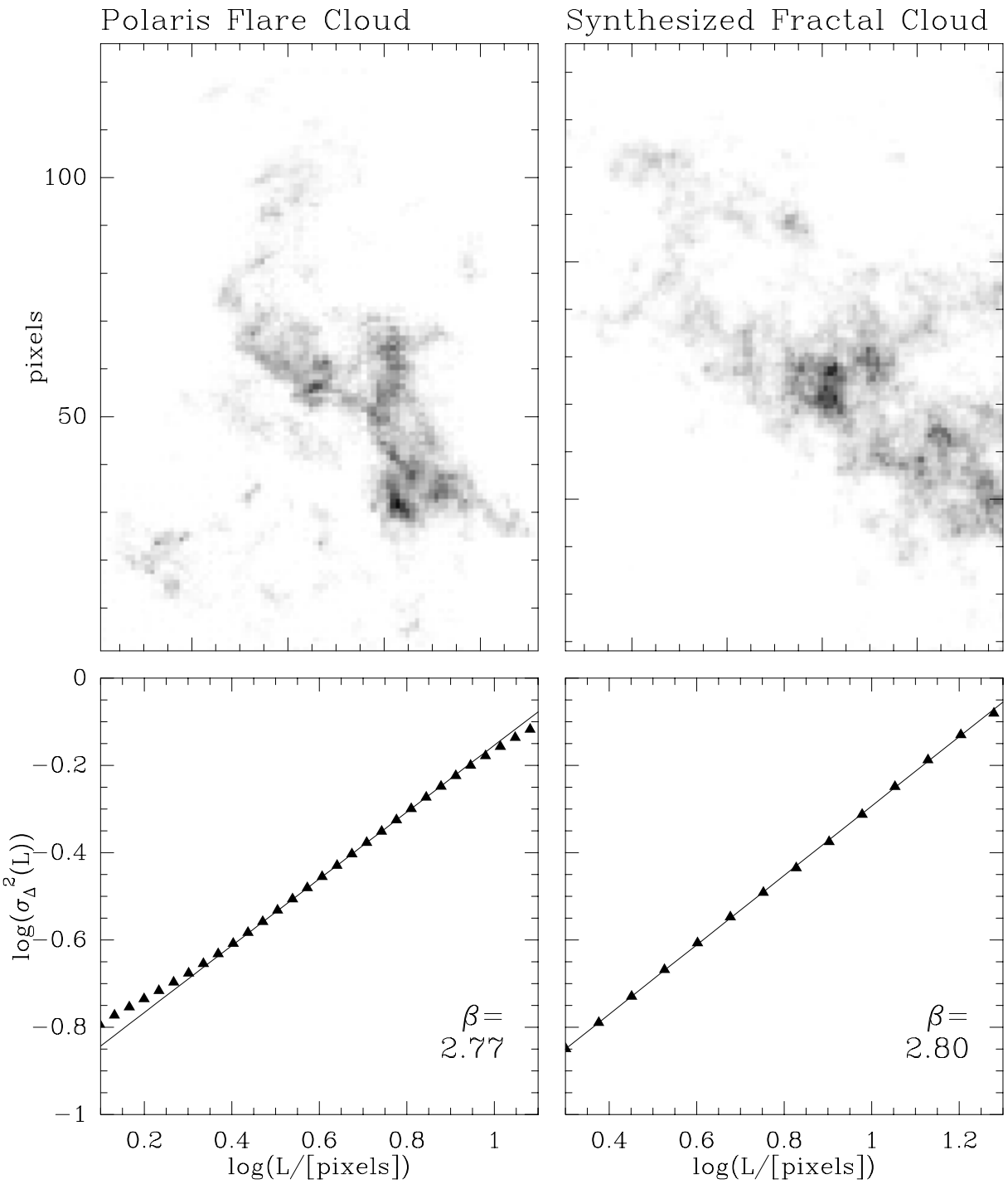

Fig. 1. Δ-*variance* analysis of an observed image of the Polaris Flare (CO $J = 1 \rightarrow 0$, 8 arcmin per pixel; Heithausen & Thaddeus (1990), top left), showing a power law behavior with an index of 0.8, which, for the 2-dimensional image corresponds to a *power spectrum* with a spectral index $\beta = 2.8$ (bottom left). The turnover into the white noise behavior at small angular scales as well as the influence of the finite image size at large scales are weakly visible (compare Fig. 3). The right hand panels show a 92 by 128 pixel subsection of a synthesized *fBm*-image (see Sect. 4) with the same *power spectrum* spectral index (top) and its corresponding Δ-*variance* behavior (bottom).

the context of characterizing the stability of atomic clocks. It has been successfully applied more recently in the analysis of the drift contributions on the resulting signal-to-noise ratio from radio astronomy receivers and backends (Schieder et al. 1989). For a random time series, the *Allan variance* on a given time scale T is basically the variance of the differences of subsequent averages over time T. The definition can easily be carried over to Fourier space, where the full information on the statistical properties of the random function is contained in its *power spectrum*. The *Allan variance* then turns out to be the filtered average of

the *power spectrum* of the noise function, weighted with the filter function $\sin^4(\pi fT)/(\pi fT)^2$. This filtering function peaks at a frequency $f \approx 1/(\pi T)$ (see Appendix A). Varying T thus allows to trace the average behavior of the *power spectrum* with frequency, which determines the drift characteristics of the signal. The *Allan variance*, representing an integral information over the *power spectrum*, however, gives much better statistical significance for the drift behavior than a single point in the *power spectrum*. In addition, it allows easy discrimination between different contributions to the random signal, such as purely white noise, flicker noise and the global drift characteristics. These properties make it useful in the analysis of drift behavior of instrumentation.

These same properties motivated us to develop a new procedure to characterize the observed 2-dimensional structure of molecular cloud images, based on the *Allan variance* concept. It is of particular importance that such a procedure should give a good discrimination between the white noise noise contribution resulting from the limited signal to noise ratio achievable for the observations and the information on the cloud structure contained in the data set.

As the literature on the *Allan variance* is rather sparse, Appendix A summarizes the definition of the *Allan-variance* for 1-dimensional random functions, discusses its relation to Fourier-analysis and in particular to the *power spectrum* in a consistent notation, and lists its characteristic properties with various types of drift behavior. With this background, extension to higher dimensions is rather straightforward. For the analysis of a 2-dim spatial structure, such as a molecular cloud image, we have to analyze the variance between differences of averages over adjacent areas with a typical spatial separation of size L. With no azimuthal direction preferred, this is naturally done in cylindrical symmetry, i.e. using a spatial filter function with a constant positive value of e.g. $+1$ on a circle of diameter L, enclosed by a ring of thickness L with a negative value of $-1/8$ (for equal weight of the two areas). In Fourier-space this corresponds to calculating the 2-dim variance as the average of the 2-dim *power spectrum* weighted with the corresponding *power spectrum* of the 2-dim filter function.

This is the concept behind the newly introduced Δ-*variance*, derived as a generalization of the 1-dim *Allan variance* in Appendix A, and defined for the analysis of random functions in higher dimensions in Appendix B. Corresponding to the $1/T$-behavior of the 1-dimensional *Allan-variance*, the 2-dimensional Δ-*variance* goes $\sigma_\Delta^2 \propto L^{-2}$ for an image dominated by purely white noise. In general, if the image has a *power spectrum* $\propto |\boldsymbol{f}|^{-\beta}$ with β in the range $0 < \beta < 6$, the 2-dimensional Δ-*variance* varies as $\sigma_\Delta^2 \propto L^{\beta-2}$ (see Appendix B).

For an observed image, the highest spatial frequency, i.e. shortest lag probed, will be close to the finite resolution, e.g. given by the Gaussian beam with a certain FWHM and a (close to) fully sampled spatial raster. The lowest spatial frequencies, i.e. largest lags, will be limited by the finite size of the cloud or of the area observed. In practice the useful limits fall at about

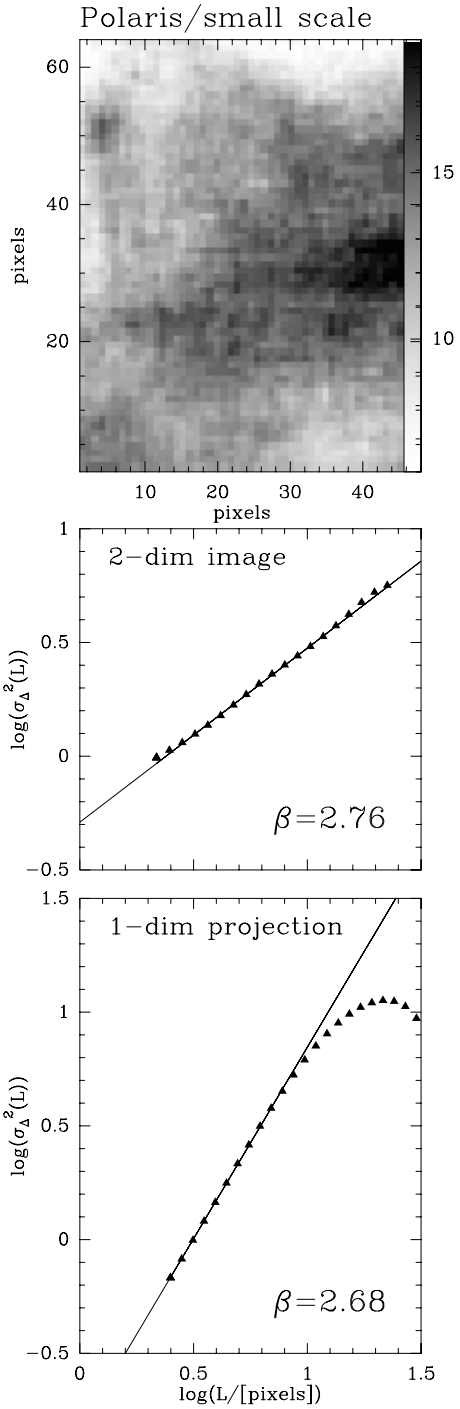

Fig. 2. Δ-*variance* analysis of a subsection of the Polaris Flare (top) observed at higher angular resolution with the IRAM 30m-telescope (CO $J = 2 \rightarrow 1$; Falgarone et al. 1998). This map covers 48 by 64 pixels, each of 7.5" extent. The image is thus zoomed in by a factor of 64 from the image in Fig. 1. The 2-dimensional Δ-*variance* analysis shows the same slope as the large scale image (Fig. 1), so that the *power spectrum* with $\beta = 2.8$ continues to these higher spatial frequencies (middle). The Δ-*variance* of the 1-dimensional projection of the same image (bottom) shows a slope by about 1 higher than that of the 2-dimensional image, as expected theoretically.

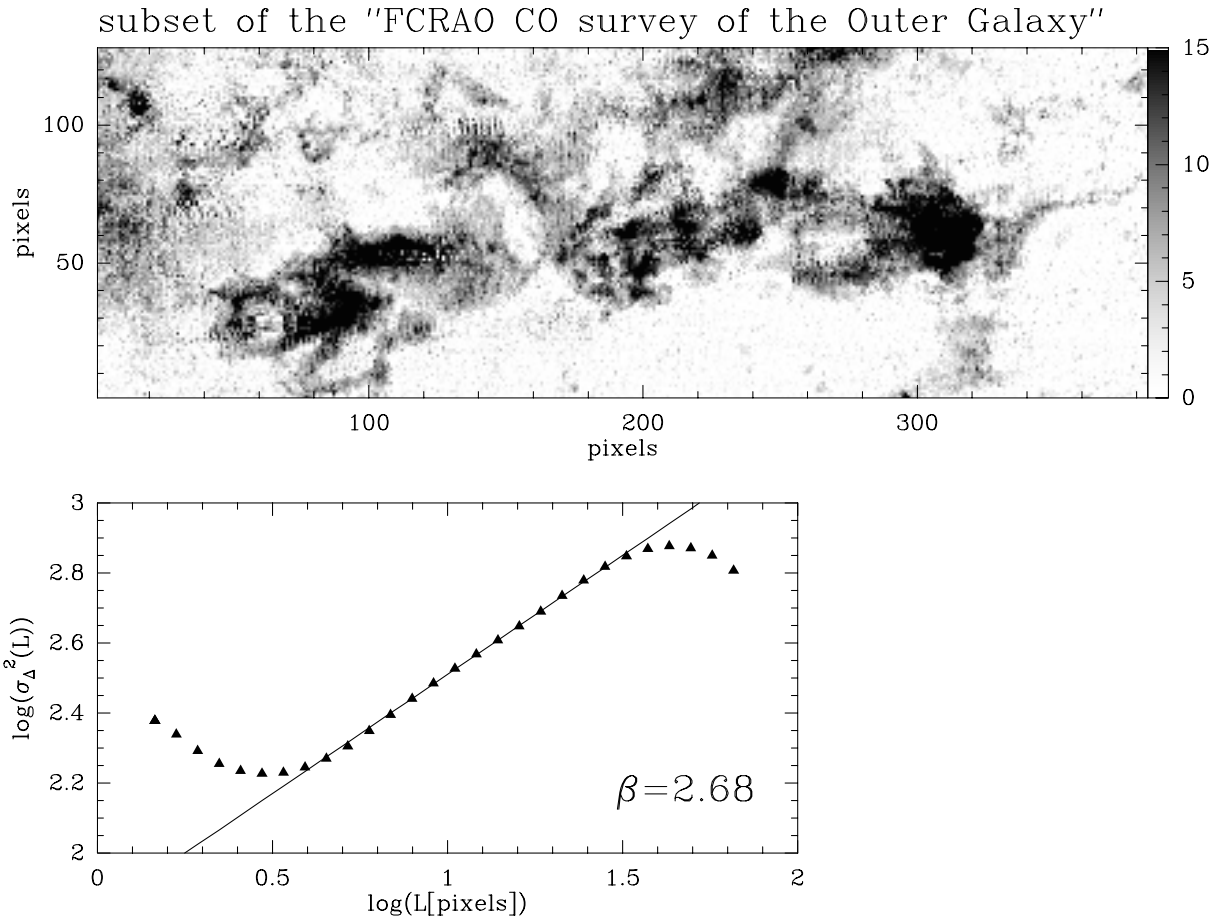

Fig. 3. Δ-*variance* analysis of a subset of the FCRAO outer galaxy survey (^{13}CO $J = 1 \rightarrow 0$; Heyer et al. 1997). This very large scale data set (384 by 128 pixels; 50" per pixel) with its relatively higher noise than the examples in Figs. 1 and 2 shows a clear turnover into the white noise behavior at the smallest angular scales, and a turnover at about a 30 pixel length scale due to the influence of the typical size of main structures in the image.

a quarter of the image size, giving at least two independent difference measures in each spatial coordinate.

2.2. Application to observed cloud images

The result of such a Δ-*variance* analysis is shown in Fig. 1, which shows the Δ-*variance* as defined above for an integrated intensity image of the Polaris Flare to closely follow a power law corresponding to a power law spectral index of $\beta = 2.8$. A small subsection of the cloud observed at higher angular resolution (observed as part of the IRAM key project "small scale structure of pre-star-forming molecular clouds", Falgarone et al. 1998) shows a very similar power law slope in the Δ-*variance* (Fig. 2). A second example is given in Fig. 3 for a subset of the FCRAO survey of the outer galaxy (Heyer et al. 1997), also giving $\beta = 2.7$. The value of $\beta = 2.8$ is remarkably close to the one measured by Green 1993, for HI clouds directly from interferometer data. Similar results can be obtained for other observed images, although the analysis often does not give as straightforward an answer as in the three examples shown. The application of the Δ-*variance* analysis to several data sets and the limitations of deriving proper variance plots from observed data sets will be presented in a separate paper (Bensch et al., *in prep.*).

2.3. Phase distribution of observed cloud images

Fig. 4 shows that the phases of the observed image are indeed randomly distributed. For one, they are uniformly distributed over the interval from 0 to π (due to the image being real valued, its *Fourier transform* is hermitian and the phases are odd, so that the phase distribution at negative values is symmetric to that at positive values). Secondly, the Δ-*variance* of the phases has a slope close to -2 as expected for a completely uncorrelated, white noise distribution (see Appendix C). Deviations from the white noise behavior may actually be significant with regard to a multifractal characteristic of the cloud image; however, they may also result from the fact that the observed image possibly has some correlation due to a (though small) extended error beam pickup. Our numerical simulations (see Sect. 4) also indicate, that the finite size of the observed image may result in deviations from the pure white noise behavior.

2.4. Discussion

The way the Δ-*variance* is defined, it implicitly averages over the angular variation in the *power spectrum*. This is due to the circular symmetry of the 2-dimensional filter function. The Δ-*variance* is thus sensitive only to the circular symmetric part of the *power spectrum* of the cloud image. The Δ-*variance* analysis shows over which range in spatial frequencies the azimuthally averaged *power spectrum* is consistent with a power law (by the straightness of the Δ-*variance* plot); and it allows, over this range, to directly derive the numerical value of the power law spectral index with high signal to noise, as it implicitly averages over the directional variation. It does not provide a measure of the degree of deviation of the *power spectrum* from spherical symmetry. Direct analysis of the azimuthally averaged *power spectrum* in principle gives the same result but makes the discrimination against the white noise contribution and finite size effects of observed images much less obvious.

One should emphasize, however, that this does not imply that the observed image has to have circular symmetry: the phases are arbitrary (and to a large degree random) and will thus cause a non circular symmetric image (the simulations presented in Figs. 1 and 3 show nice examples for this). One should keep in mind, however, that the Δ-*variance* method should be applied with care to images which obviously are dominated by systematic large scale structure, e.g. showing a preferred direction, like a large scale filament broken up into a series of clumps on preferred length scales, or a sharp cloud boundary resulting from e.g. shock interaction.

Instead of analyzing the 2-dimensional image, one can investigate its 1-dimensional projection. The projection results from the integration along a given direction, e.g. along the x-axis. The *Fourier transform* of the projected 1-dimensional strip is the value of the 2-dimensional *Fourier transform* at the $f_x = 0$ axis. For a power law *power spectrum* $\mathcal{P}(f) \propto (f_x^2 + f_y^2)^{-\beta/2}$ in 2 dimensions, the 1-dimensional projection thus has a *power spectrum* $\mathcal{P}(f_y) \propto (f_x^2 + f_y^2)^{-\beta/2}\big|_{f_x=0} = f_y^{-\beta}$. The power law index of the *power spectrum* of the 1-dimensional projection is thus the same as that of the 2-dimensional image. This result holds equally well for higher dimensional images: the $(E-1)$-dimensional projection of an E-dimensional structure with a power law *power spectrum* has again a power law *power spectrum* with the same spectral index. With the general relation between the *power spectrum* index β and the power law index of the E-dimensional Δ-*variance* $\sigma_\Delta^2 \propto L^{\beta-E}$ as given in Appendix C, we thus expect the projection of a 2-dimensional image with *power spectrum* index β, i.e. 2-dimensional Δ-*variance* index $\beta-2$, to have a 1-dimensional Δ-*variance* index $\beta-1$. Fig. 2 (bottom) shows as an example the result for the high angular resolution data set of the Polaris Flare observed with the IRAM 30m telescope. We note, however, that other clouds analyzed in the same way show Δ-*variance* results for the 1-dimensional projections that are not consistent with the values expected from the analysis of the 2-dimensional images; this is likely due to real data sets being limited by finite size and other systematic effects, as we will discuss in detail in Bensch et al. (*in prep.*).

3. Connection with the theory of fractal images

It is well established within the work that has been done in analyzing and synthesizing fractal images (e.g. in order to generate artificial landscapes for computer animations etc.), that such structures can easily be generated as so called *fractional Brownian motion* (*fBm*)-images (see e.g. Peitgen & Saupe 1988). These are generated by specifying a power law *power spectrum* with a given index $\beta = E + 2H$, where E is the Euclidean dimension of the image and H, the *drift exponent* (see below; sometimes also called *Hurst exponent*) ranges between 0 and 1, and completely random phases of the image [1]. Such structures have a *two point correlation function*

$$G_s(\boldsymbol{\rho}) = G_s(|\boldsymbol{\rho}|) = \langle (s(\boldsymbol{r}+\boldsymbol{\rho}) - s(\boldsymbol{r}))^2 \rangle \propto \rho^{2H} = \rho^{\beta-E}$$

as derived in Appendix B, where $s(\boldsymbol{r})$ is the signal, i.e. image intensity. The drift behavior (mean variation over distance) is correspondingly $\Delta s(\rho) = \sqrt{G_s(\rho)} \propto \rho^H$. Note that the range for $\beta = E + 2H$ with H between 0 and 1 spans exactly the regime from $\beta = E$ to $\beta = E+2$ for which the E-dimensional *two point correlation function* follows the $\rho^{\beta-E}$ behavior (see Appendix B). Outside the *fBm*-range, it turns, for higher values of β, over into a behavior $\propto \rho^2$, independent of the value of β. For smaller values of β, the *two point correlation function* does not have a simple power law behavior for small ρ.

The drift behavior of an *fBm* structure, $\Delta s(\rho) \propto \rho^H$, implies a fractal dimension of the E-dimensional "mountain surface" $s(\boldsymbol{r})$ of $d_H = E + 1 - H$, e.g. measured as a box coverage dimension (see Voss 1988): at a linear scale ρ a single $E+1$-dimensional box of volume $V(\rho) = \Delta s(\rho)\, \rho^E$ is needed to enclose the "mountain surface". At a δ times smaller scale $\delta\rho$ each enclosing box has a volume of $V(\delta\,\rho) = \Delta s(\delta\,\rho)\,(\delta\,\rho)^E = \delta^{H+E}\, V(\rho)$, and $1/\delta^E$ such boxes are needed to enclose the "mountain surface" over the original extent. These boxes thus cover a total volume of $\delta^H\, V(\rho)$. In units of scaled down original boxes, each having a volume of $\delta^{E+1}\, V(\rho)$, one thus requires $N(\delta) = 1/\delta^{E+1-H}$ of such boxes to enclose the "mountain range". According to the definition of the box-coverage fractal dimension d_H, $N(\delta) \propto 1/\delta^{d_H}$, so that comparison with the above results shows that $d_H = E + 1 - H$.

Inserting the above relation between β and H, namely $\beta = E+2H$, we get $d_H = (3E+2-\beta)/2$ as the relation between the fractal dimension of the *fractional Brownian motion* structure and the power law index of its *power spectrum*. As expected, d_H thus varies between $E+1$ and E for β varying between E and $E+2$. Outside this range, d_H settles at these extreme values according to the settling of the drift behavior at $H = 0$ and $H+1$ for too small and too large power law indices β.

As was discussed in the previous section, the $(E-1)$-dimensional projection of an E-dimensional structure with a

[1] note the slightly different definition of β used here in comparison to Peitgen & Saupe (1988), where ours includes the Euclidean dimension E within β.

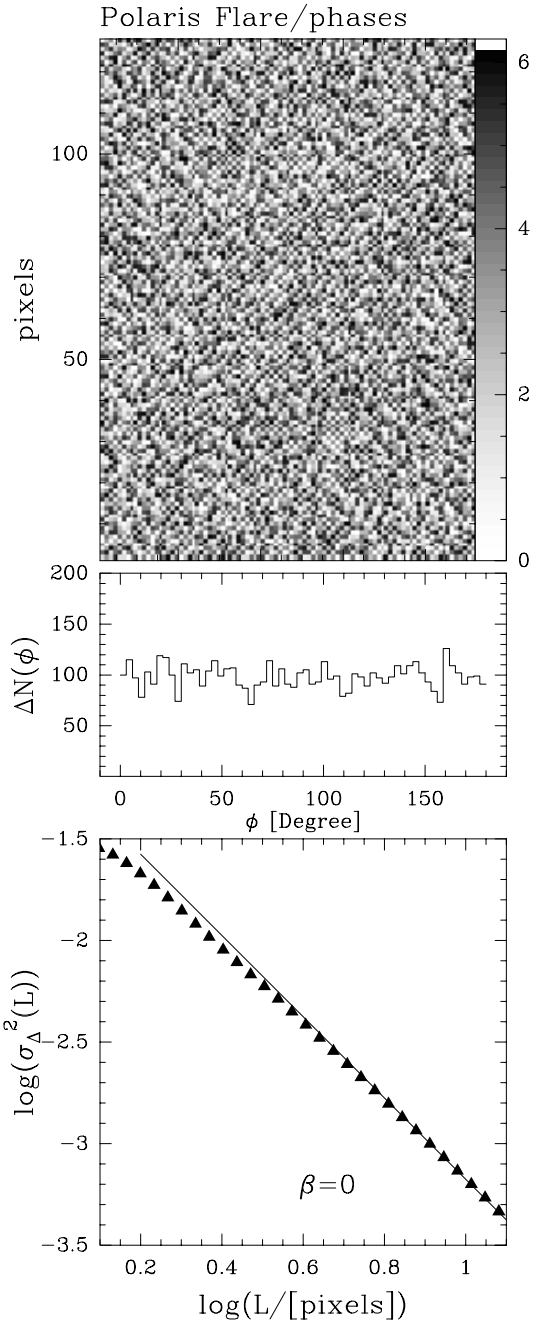

Fig. 4. The phases (top) of the Polaris Flare image shown in Fig. 1: the distribution of the phases is uniform (center); the Δ-*variance* of the phases shows a close to white noise behavior, i.e. a slope of -2, corresponding to $\beta = 0$ (bottom).

power law *power spectrum* has again a power law *power spectrum* with the same spectral index (note that in the case of infinitely extended images, this is even independent of whether the phases are randomly distributed or not). The randomness of the phases for the E-dimensional image implies randomness of the phases of the projected $(E-1)$-dimensional image, as is obvious from the fact that the phases in the $k_z = 0$-plane of the E-dimensional Fourier image are randomly distributed. The fact that β stays constant on projection is in contrast to the commonly formulated, though never proven, hypothesis, that the fractal dimension of the projection of a fractal structure is lower by 1 than that of the original structure. With the relations between the various parameters of an *fBm*-structure as discussed above, we explicitly show that this does not hold for a *fractional Brownian motion* fractal structure. The fact that the *power spectrum* spectral index $\beta = E + 2H_E$ stays constant on projection implies that the drift index H_E changes: from $\beta = E + 2H_E = (E-1) + 2H_{E-1}$ we conclude that $H_{E-1} = H_E + 1/2$. The fractal dimension as defined above then changes from $d_{H_E} = E + 1 - H_E$ to $d_{H_{E-1}} = (E-1) + 1 - H_{E-1} = d_{H_E} - 3/2$, that is by 1.5, and not by 1.

This implies that a *fractional Brownian motion* structure becomes smoother, i.e. gets closer to the limit of a regular Euclidean structure ($d_H = E$, $H = 1$), on each projection. Even if it starts out in E dimensions close to being very broken up, with H close to 0, i.e. $H = 0 + \epsilon$, the first projection, that is the $E-1$-dimensional structure has already $H = 0.5 + \epsilon$; and after the second projection the resulting $E-2$-dimensional structure formally has already $H = 1 + \epsilon > 1$. Its power law index thus falls outside the range where $G(\rho) \propto \rho^{\beta - E}$; the drift behavior rather settles at $G(\rho) \propto \rho^2$, i.e. $H = 1$. A *fractional Brownian motion* structure can thus be projected at maximum once before becoming smooth enough to be indistinguishable from a Euclidean structure: on projection, the small scale structure overlaps to form larger, smoother structures.

Another measure of the fractal dimension of e.g. a 2-dimensional image is given by the area-perimeter relation of its iso-intensity contours, which scale as $perimeter \propto area^{d/2}$. For these 1-dimensional structures the fractal dimension d varies between $d = 1$ in the Euclidean limit ($perimeter \propto \sqrt{area}$) up to the maximum value of $d = 2$, where the perimeter increases linearly with the area enclosed. Similarly for a 3-dimensional structure: consider a 3-dimensional fractal density distribution; the area of its iso-density 2-dimensional surfaces scales with their enclosed volume as $surface\ area \propto volume^{d/3}$, with d ranging between 2 and 3.

Voss (1988), p. 65, states that in general, given an E-dimensional *fractional Brownian motion* density structure with $\beta = E + 2H$ and correspondingly a box coverage fractal dimension $d_H = E + 1 - H$, its $E-1$-dimensional iso-density surfaces, being effectively "zero-cuts" of the E-dimensional structure, have an area-perimeter (resp. volume-surface) fractal dimension $d = d_H - 1$ by exactly 1 lower than the box coverage fractal dimension of the structure they result from. Vogelaar & Wakker (1994) checked this numerically over a limited range of β by analyzing *fBm*-structures generated to calibrate their area-perimeter relation code. We developed a similar code (Zielinsky et al., *in prep.*) and also compared various numerical methods to determine the area and perimeter of contour lines. Within the systematic errors associated with each method, the area-perimeter fractal dimension of the Polaris Flare image shown in Fig. 1 is $d \approx 1.6$ or slightly higher, consistent with the fractal parameters determined by the other methods discussed above. Note that this value for the fractal dimension is higher than that

determined for several other clouds in various tracers, which typically gives values in the range 1.3 to 1.5.

At this place a cautioning remark seems appropriate, encouraging careful distinction between the different *fractal dimensions* in use. To illustrate this, consider a 3-dimensional *fBm* density structure with a certain value of $\beta = 3 + 2H_3$. Its box coverage dimensions as defined above is then $d_H = 4 - H_3$, the (volume-surface) dimension of its 2-dimensional iso-density surfaces is correspondingly by 1 lower, i.e. $d = d_H - 1 = 3 - H_3$. Due to the constancy of β on projection, the corresponding 2-dimensional column density image has, as derived above, $H_2 = H_3 + 1/2$; its box coverage dimension is $d_H = 3 - H_2$, and is 3/2 less than that of the 3-dimensional structure. The (area-perimeter) dimension of the (1-dimensional) iso-column-density contours is again by 1 lower than the box coverage dimension of the 2-dimensional column density structure, $d = d_H - 1 = 2 - H_2$, and thus also 3/2 less than the (volume-surface) dimension of the (2-dimensional) iso-density surfaces.

Table 1 summarizes the connection between the different parameters. It also includes the range of parameters derived from observations of the Polaris Flare in the present paper. The values for the Polaris Flare are in very good agreement with the relations derived for an *fBm* structure and a value of H near 0.4.

4. Generating artificial molecular cloud images

The concept of *fractional Brownian motion* structures allows easy generation of synthetic images. Various methods are discussed in Peitgen & Saupe (1988). We generated synthesized images in the following way: specify the power law index β of the *power spectrum*; for an image with $n \times n$ pixels calculate the Fourier amplitudes at the n^2 spatial frequency points in the Fourier domain $\propto 1/f^{\beta/2}$ (according to the $1/f^{\beta}$ *power spectrum* power law), and select completely random phases, i.e. uniformly distributed over the interval $[0, 2\pi)$ with a random number generator. As the image should be real valued, the Fourier amplitudes and phases have to match the appropriate symmetry conditions of hermiticity, $\bar{s}(\boldsymbol{f}) = \bar{s}^*(-\boldsymbol{f})$. With the circular symmetry of the *power spectrum*, and hence the Fourier amplitudes, this results in the condition for the phases to be odd: $\varphi(\boldsymbol{f}) = -\varphi(-\boldsymbol{f})$. This is most easily realized in a numerical simulation by first generating an unconditioned set of phases, $\chi(\boldsymbol{f})$, from which the odd phases are generated as $\varphi(\boldsymbol{f}) = \chi(\boldsymbol{f}) - \chi(-\boldsymbol{f})$. *Fourier transform* (or fast Fourier transform, FFT, in case the number of points in each dimension matches 2^n) then generates the *fBm*-image.

A slight complication arises when we deal with intensity images, like those of molecular line maps. In this case the image values have to be positive definite at all points. As there is no prescription on how to select Fourier amplitudes and phases in order to get a positive definite image, this condition is not easy to match. One possibility is to simply add an offset to the resulting image, so that its minimum value is equal to 0. This approach is, however, rather arbitrary. A second approach is based on the fact that the square of a real valued image is always positive definite. Squaring the image corresponds to self-convolution in the Fourier-domain. For an *fBm* image, squaring preserves the power law shape of the *power spectrum* and its spectral index, though only on average: considering the fact that the phases are completely random, it is plausible that the convolution process, i.e. the coherent adding up of the image amplitudes for all possible spatial lags, leads to close cancellation for all spatial lags except for the 0-lag point (and the points with appropriate symmetry). The amplitudes are reproduced, but with a random fluctuation due to the near cancellation of the random phases. We verified this by analyzing synthesized images generated this way. A proper proof would be highly desirable, but has to await future work.

The result crucially depends on the randomness of the phases in the original image. Due to the self-convolution in the Fourier-domain, this procedure is sensitive to possible aliasing effects. This complication results from the unavoidable periodic repetition of the Fourier transform due to the discrete sampling of a numerical realization of an image. The effect is the weaker, the steeper the *power spectrum*, i.e. the higher the value of β. The magnitude of the *power spectrum* in the overlap region is then correspondingly lower. Large pixel numbers also help, as they increase the dynamic range over which the power law *power spectrum* gets sampled. In our numerical simulations, pixel numbers of at least 64 in each dimension turned out to be sufficient for *fBm*-images not too close to the ones with the most shallow *power spectrum* possible, i.e. $\beta = E$. For pixel numbers of 256 in each dimension, still easy to handle even for 3-dimensional images, these aliasing effects turned out to be clearly confined to only the lowest spatial frequencies. The Δ-*variances* of the images generated still show a wide range in spatial lags which follow the theoretical power law behavior derived in Appendix C.

Other methods for generating artificial fractal structures such as creating log-normal random distributions of density fluctuations, e.g. applied when synthesizing multifractals or often used in simulating primordial cosmological density fluctuations, might be used, but would have to be carefully checked with regard to the randomness of the phases of the resulting images, crucial in order for them to represent true *fractional Brownian motion* structures.

Fig. 1 (right side) shows an example of an *fBm*-structure generated this way, where we choose $\beta = 2.8$, close to the value derived from the observed image of the Polaris Flare. In addition, we varied the seed value of the random number generator used for generating the random phases until we obtained an image whose large scale structure accidentally resembles the Polaris Flare section displayed in Fig. 1 (left). The comparison shows that such a structure actually gives a good representation of the structure observed for molecular cloud images.

Fig. 5 shows a series of synthesized *fBm* images covering the full range of $H = 0 \ldots 1$, i.e. $\beta = 2 \ldots 4$. Considering the pixel size of these synthesized images as the resolution of the maps, simple eye inspection of this series shows them to be most similar to real molecular cloud images for β in the range $2.8 \ldots 3.2$, in good agreement with the value derived above from the Δ-*variance* analysis. This test, though admittedly not a quanti-

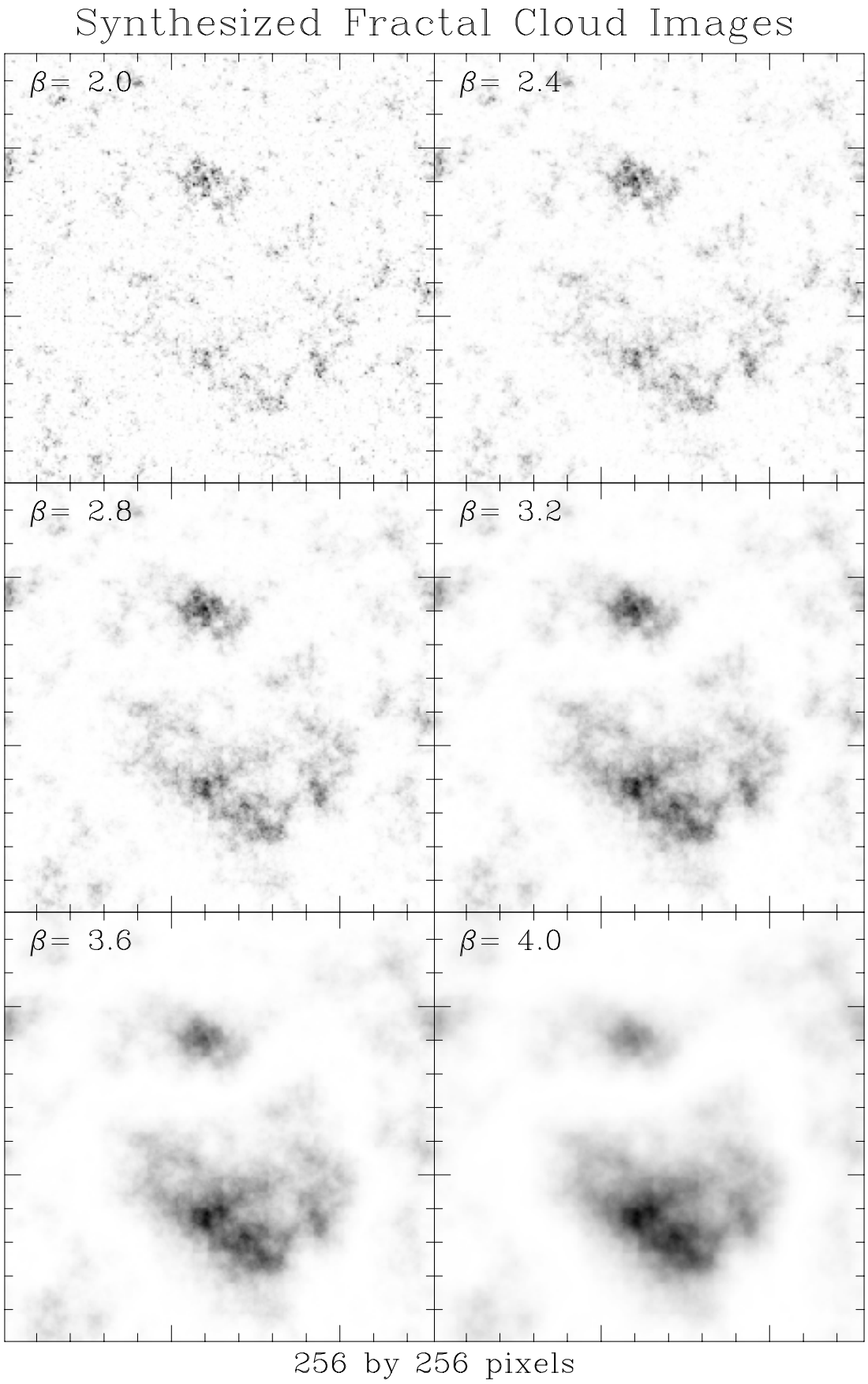

Fig. 5. A series of synthesized 256×256 pixel *fBm*-images, varying the power law spectral index between $\beta = 2 \ldots 4$ in steps of 0.4. The random number series generating the phases has been kept constant between the images.

Table 1. Fractal parameters characterizing Molecular Clouds

		defining relation	relation with H	allowed range for *fBm*-structure	Polaris Flare cloud ($E = 2$)
power spectrum spectral index	β	$\mathcal{P}(f) \propto \lvert\boldsymbol{f}\rvert^{-\beta}$	$\beta = E + 2H$	$\beta = E \ldots E + 2$	$\beta \approx 2.8$
drift behavior	H	$\Delta s(\rho) \propto \rho^H$		$H = 0 \ldots 1$	$H \approx 0.4$
box coverage dimension	d_H	$N(\delta) \propto 1/\delta^{d_H}$	$d_H = E + 1 - H$	$d_H = E + 1 \ldots E$	
area-perimeter relation($E = 2$) volume-surface relation($E = 3$)	d	$p \propto a^{d/2}$ $a \propto v^{d/3}$	$d = E - H$	$d = E \ldots E - 1$	$d \approx 1.6$
clump-mass spectral index	α	$dN/dM \propto M^{-\alpha}$	$\beta = \gamma(3 - \alpha)$ where $M \propto r^\gamma$	$\alpha = 3 - \frac{E}{\gamma} \ldots 3 - \frac{E+2}{\gamma}$	$\alpha \approx 1.8$ $\gamma \approx 2.3$

tative analysis, has been performed successfully with several experienced molecular cloud observers.

5. Power spectrum of the image of an ensemble of randomly positioned clumps with a power low mass spectrum

The complex structure of molecular clouds is often described as clumpy. This phrasing assumes that the structure is actually composed of discrete entities, i.e. clumps, making up the cloud. In projection, the many individual clumps along the line of sight overlap and it would be difficult to identify individual clumps in projected, integrated intensity maps. Due to the interclump velocity dispersion the observed molecular cloud intensity distribution can, however, be decomposed into clumps, i.e. substructures coherent in their spatial and velocity distribution. As long as the observation is done in an optically thin line, the integrated intensity of the thus identified clumps is directly proportional to the clumps mass. In this way, one can measure the clump mass distribution of a molecular cloud.

The two methods to identify clumps via automated procedures that have been published in the literature (Stutzki & Güsten 1990; Williams et al. 1994) differ in how they define clumps. They nevertheless agree, together with several other results on clump mass spectra based on eye inspection of molecular line maps, in that the observed clouds have a clump mass spectrum of the shape $dN/dM \propto M^{-\alpha}$, with α in the range 1.6 to 1.8 for most clouds (Kramer et al. 1998). There is a tendency that the higher quality data sets tend to give steeper mass spectra, i.e. α closer to 1.8. This is expected as with lower signal to noise ratio the decomposition has more difficulty in separating smaller clumps that almost merge with larger ones (see Kramer et al. (1998) for a detailed comparison of the various methods for clump decomposition described in the literature).

Although the concept of dividing the observed structure into discrete subentities seems to be almost orthogonal to analysing the structure in terms of fractal dimension or *power spectra*, we will now show that the two concepts are actually closely connected, and that the clump mass spectral index α and the *power spectrum* power spectral index β of the 2-dimensional projected image are connected.

5.1. *fBm*-structure of a clump ensemble with a power law mass spectrum

In order to establish a link between the clumps mass distribution and the spatial structure of the image of the clump ensemble, one has to assume in addition a relation between the clump mass and size, $M \propto r^\gamma$, where $\gamma = 3$ represents clumps with on average constant clump volume density, and $\gamma = 2$ represents clumps with on average constant clump column density. The latter case corresponds to a clump density $n \propto \Delta r^{-1}$ and is commonly referred to as one of Larson's relations (Larson 1992).

We assume the clumps to have Gaussian shape. Though actual clumps are likely to have more complex shapes, the assumption of Gaussian clumps is convenient for the mathematical derivation in the following, and is not critical for the connection between the clump mass spectral index and the *power spectrum* power law index to be derived, as will be discussed below.

We consider an ensemble of randomly positioned, Gaussian shaped clumps with a mass spectrum $dN/dM = AM^{-\alpha}$, with $1 < \alpha < 2$, a high mass cutoff M_h, and a low mass cutoff M_l. The restriction $\alpha < 2$ guarantees the mass to be dominated by the high mass clumps. Assuming $M_h \gg M_l$, the total mass is thus determined by the high mass cutoff,

$$M_{tot} = \frac{A}{2-\alpha} M_h^{2-\alpha} \left[1 - \left(\frac{M_l}{M_h}\right)^{2-\alpha}\right] \approx \frac{A}{2-\alpha} M_h^{2-\alpha}.$$

The restriction $\alpha > 1$ implies the total number of clumps to be dominated by the low mass clumps, so that the total number of clumps is determined by the low mass cutoff,

$$N_{tot} = \frac{A}{(\alpha-1)M_l^{\alpha-1}}\left[1-\left(\frac{M_h}{M_l}\right)^{1-\alpha}\right] \approx \frac{A}{(\alpha-1)M_l^{\alpha-1}}$$

(note that α should not be too close to either 1 or 2 in order for these approximations to be valid).

A Gaussian shaped clump, i.e. a clump with a Gaussian density distribution, has as well a Gaussian column density distribution in projection, and hence, for an optically thin line and uniform excitation conditions, a Gaussian intensity distribution on the sky. The intensity for a single clump, centered at $\boldsymbol{x}_0$, with peak intensity I_0 and size Δr (FWHM) is thus given by

$$I(\boldsymbol{r}) = I_0 \exp\left[-\frac{4\ln 2(\boldsymbol{r}-\boldsymbol{r}_0)^2}{\Delta r^2}\right]$$

and leads to a Gaussian shaped *Fourier transform* of the intensity,

$$\tilde{I}(\boldsymbol{f}) = \tilde{I}_0 \exp\left[-\frac{4\ln 2 f^2}{\Delta f^2}\right]\exp(2\pi i \boldsymbol{f}\cdot\boldsymbol{r}_0)$$

where the peak amplitude in Fourier space is the integral in the image domain, i.e. is proportional to the spatially integrated clump intensity, and hence the clump mass (as long as the clump density is above the critical density): $\tilde{I}_0 = \mu M_{cl}$. The constant of proportionality μ depends on the details of the molecular species and transition observed as well as on its abundance. The width of the clump in Fourier space is inversely proportional to its FWHM in the image domain: $\Delta f = \frac{4\ln 2}{\pi}\frac{1}{\Delta r}$. The non zero center position of the clump results in the phase factor $\exp(2\pi i \boldsymbol{f}\cdot\boldsymbol{r}_0)$.

Using the above relation between clump mass and size, $M_{cl} = c_\gamma \Delta r^\gamma$, we can then substitute the clump size by the clump mass and obtain for the *Fourier transform* of an individual clump

$$\tilde{I}_{cl}(\boldsymbol{f}) = \mu M_{cl}\exp\left[-f^2\delta M_{cl}^{2/\gamma}\right]\exp(2\pi i \boldsymbol{f}\cdot\boldsymbol{r}_0),$$

where we have introduced the abbreviation $\delta = \frac{\pi^2}{4\ln 2\ c_\gamma^{2/\gamma}}$.

The total image is then the sum of the images of the individual clumps. As the *Fourier transform* is linear, the same holds for the *Fourier transform* of the clumpy cloud image:

$$\begin{aligned}\tilde{I}(\boldsymbol{f}) &= \sum_i \tilde{I}_{cl,i}(\boldsymbol{f}) \\ &= \mu\sum_i M_i \exp(-f^2\delta M_i^{2/\gamma}) exp(2\pi i \boldsymbol{f}\cdot\boldsymbol{r}_{0,i}).\end{aligned}$$

The *power spectrum* of the clumpy cloud image is the square of the *Fourier transform*:

$$\begin{aligned}&|\tilde{I}(\boldsymbol{f})|^2 = \\ &\mu^2\sum_{i,j} M_i M_j \exp\left[-f^2\delta\left(M_i^{2/\gamma}+M_j^{2/\gamma}\right)\right] \\ &\times\cos\left(2\pi\boldsymbol{f}\cdot(\boldsymbol{r}_{0,i}-\boldsymbol{r}_{0,j})\right).\end{aligned}$$

Due to the randomness of the clump positions, i.e. the randomness of the phases in the *Fourier transform*, the mixed terms, i.e. those with $i \neq j$ in this sum average out to zero. This approximation is the better, the more clumps we average over. It only holds for sufficiently large f, a condition guaranteed anyway by the limitations for f given below. Only the terms with $i = j$, i.e. those with the square of the *Fourier transform* of an individual clump, have zero phase and thus remain. To a good approximation, we can then replace the square of the sums by the sum of the squares:

$$|\tilde{I}(\boldsymbol{f})|^2 \approx \mu^2\sum_i M_i^2\exp(-2f^2\delta M_i^{2/\gamma}).$$

The sum can now be approximated by an integral over clump masses by introducing the mass distribution of the clumps $dN/dM = (2-\alpha)\frac{M_{tot}}{M_h^{2-\alpha}}M^{-\alpha}$. This gives

$$\begin{aligned}|\tilde{I}(\boldsymbol{f})|^2 &= \int_{M_l}^{M_h}\mu^2 M^2\exp(-2\,f^2\,\delta\,M^{2/\gamma})\,\frac{dN}{dM}dM \\ &= (2-\alpha)\frac{M_{tot}}{M_h^{2-\alpha}}\mu^2\int_{M_l}^{M_h} M^{2-\alpha}\exp(-2\,f^2\,\delta\,M^{2/\gamma})\,dM.\end{aligned}$$

Substituting $z = f\,M^{1/\gamma}$ gives an expression, where the f-dependence is completely outside the integral, except for the dependence through the lower and upper mass cutoff:

$$\begin{aligned}&|\tilde{I}(\boldsymbol{f})|^2 = \\ &\frac{\gamma\,(2-\alpha)\,\mu^2\,M_{tot}}{M_h^{2-\alpha}}\,f^{-(3-\alpha)\gamma}\int_{fM_l^{1/\gamma}}^{fM_h^{1/\gamma}} z^{(3-\alpha)\gamma-1}\exp(-2\delta z^2)dz.\end{aligned}$$

One can easily see that the f-dependence through the integration boundaries can be neglected for spatial frequencies f well above the shortest, and well below the largest spatial frequencies, corresponding to the high and low mass cutoff respectively. At the upper integration boundary $z_h = f\,M_h^{1/\gamma}$, the error made in moving the boundary towards ∞ approaches zero as long as the argument of the exponential function in the integrand is much larger than unity, i.e. $2f^2\delta M_h^{2/\gamma} \gg 1$, thus $f \gg \frac{1}{\sqrt{8\ln 2}}\Delta f(M_h)$. In the range of $\alpha < 3$ the integral rapidly converges toward a constant value at the lower boundary as long as the argument of the exponential function in the integrand is small there, i.e. $f \ll \frac{1}{\sqrt{8\ln 2}}\Delta f(M_l)$. Extending the integration boundaries to 0 and infinity is thus a good approximation as long as $\frac{1}{\sqrt{8\ln 2}}\Delta f(M_l) \gg f \gg \frac{1}{\sqrt{8\ln 2}}\Delta f(M_h)$. The resulting integral converges and can actually be evaluated in closed form. The complete frequency-dependence of the *power spectrum* is in the trailing term:

$$|\tilde{I}(\boldsymbol{f})|^2 \approx \frac{\gamma\,(2-\alpha)\,\mu^2\,M_{tot}}{M_h^{2-\alpha}}\,\frac{\Gamma\left(\frac{\gamma}{2}(3-\alpha)\right)}{2\,(2\delta)^{\frac{\gamma}{2}(3-\alpha)}}\,f^{-(3-\alpha)\gamma},$$

We see that the *power spectrum* is indeed of power law shape. The spectral exponent is $\beta = (3-\alpha)\,\gamma$.

Whereas we have assumed an exact relation between clump mass and size in the above derivation, one can easily see that it holds as well for a distribution of clumps

which satisfy the mass-size relation only on average: the individual clump properties simply have to be replaced by their average properties in each mass bin. Also, though we derived the result for spherical clumps, it extends straightforwardly to randomly oriented elliptical clumps. We should also note that, although we assumed Gaussian shaped clumps, the relation will hold as well for other shapes, as long as the *power spectrum* of an individual clump image drops with a power law exponent higher than $\beta = (3-\alpha)\gamma$, so that the upper integration boundary can be extended to infinity.

Repeating the derivation above for the 3-dimensional density distribution shows that its *power spectrum* power law index, rather than that of the 2-dimensional projection derived above, also turns out to be $\beta_3 = (3-\alpha)\gamma$. This result is immediately obvious considering the fact derived in Sect. 3 that the power law spectral index of the *power spectrum* does not change on projection.

5.2. Comparison with observations

Let us now compare and discuss the numerical values derived for the various parameters from observational data and their agreement with the relation derived. For the case $\gamma = 2$, i.e. assuming on average constant clump column density, we obtain $\beta = 6 - 2\alpha$; for the case $\gamma = 3$, i.e. assuming on average constant volume density, the relation would be $\beta = 9 - 3\alpha$. For the typical range of α between 1.6 to 1.8 observed in molecular clouds (as discussed above), we obtain a range of values for β between 3.8 to 2.4 for the case $\gamma = 2$, and between 4.2 to 3.6 for the case $\gamma = 3$. The former is in accordance with the observed value of β around 2.8, the latter is clearly too high, thus favoring a value of γ closer to 2.

The value of γ is usually determined observationally by a fit to the mass and size values of the clumps identified in a given data set. Clump sizes are difficult to determine and the actual values will depend on the method used to identify clumps. This is different from the determination of clump masses, which, being derived as the integral over the spatial and velocity coordinate of the observed intensity distribution are a much more robust quantity and in particular independent of the resolution of the observations (Kramer et al. 1998). In addition the relatively small coverage of linear spatial scales even for relatively large molecular cloud maps and the systematic effects coming in close to the resolution limit make the determination of the mass-size index marginal for each single set of observations. Values for γ determined from individual data sets typically range from 2.5 up to 3.3 (Elmegreen & Falgarone 1996) and the mass-size plots often show systematic curvatures beyond a simple power law behavior. A smaller value and a better correlation is obtained when combining various observations covering a larger range of angular scales for a particular source. This has been done for the Polaris Flare data (Heithausen et al. 1998), which gives $\gamma = 2.3$ (and $\alpha = 1.8$ for the clump mass spectral index), presumably providing the most consistent determination up to date of these parameters within a single molecular cloud complex. An identical value of γ is obtained by combining a large set of data from different sources in the recent analysis by Elmegreen & Falgarone (1996). The values determined from individual data sets are thus systematically larger than the ones from data sets combining observations with different angular resolution and source distances. This indicates that the larger values obtained for the individual surveys are likely to be biased by resolution effects and other systematic errors of the clump size determination in the clump identifying procedure.

The relation derived above between the mass spectral index α, the *fBm*-index β and the mass-size relation index γ can be used to determine γ from the measured values of α and β, independently and without relying on the actual values of the sizes derived for individual clumps. For the Polaris Flare, used as the prime example within this paper, we then get $\gamma = \frac{\beta}{3-\alpha} = 2.3$, in perfect agreement with the value derived by Heithausen et al. (1998) from the combination of small and large scale observations.

To summarize, there is good support for the concept, that the different methods of analyzing molecular cloud structure, including the determination of clump mass spectra and their spectral index, simply describe different aspects of the same underlying physical structure, which is characterized by a power law *power spectrum* of otherwise random density fluctuations. The derived relation between mass spectral index α and *fBm*-index β, $\gamma = \frac{\beta}{3-\alpha}$ can be used to independently determine the power law index γ of the mass-size relation.

6. The relation between mass spectrum, size spectrum, mass-size relation and fractal dimension

The relations established in the preceding sections link the indices of the clump mass spectrum and the clump size spectrum, together with the power law index of the mass-size relation of the clumps, with the fractal dimension of the image of the clump ensemble. These relations will be discussed in the next two subsections, together with a critical analysis of similar relations discussed in the literature, that are based on a different fractal cloud model.

6.1. The clump mass spectrum and the fractal dimension

With the relation between the power law mass spectral index α of an ensemble of clumps and the power spectral index β of its 2-dimensional projection as derived above, $\beta = (3-\alpha)\gamma$, we can now connect the mass spectral index α with the drift index H and the fractal dimension d_H of the projected image:

$$\alpha = 3 - \frac{\beta}{\gamma} = 3 - \frac{2+2H}{\gamma} = 3 - \frac{8-2d_H}{\gamma}.$$

We recall from Sect. 3 that for an *fBm*-structure with power law index $\beta = E + 2H$ to have drift behavior $\langle (s(\boldsymbol{r}+\boldsymbol{D}) - s(\boldsymbol{r}))^2 \rangle \propto D^{2H}$ or a fractal dimension $d_H = E + 1 - H$, the value of H is limited to the range $0 \ldots 1$. β thus has to be in the range $E \ldots E+2$. The range $H = 0 \ldots 1$ corresponds to α ranging from $3 - \frac{2}{\gamma} \ldots 3 - \frac{4}{\gamma}$. For the case

$\gamma = 2$, α ranges from $2 \ldots 1$. For $\gamma = 3$ the proper range would be $\alpha = 2\frac{1}{3} \ldots 1\frac{2}{3}$. Reversely, for the case of on average constant column density, $\gamma = 2$, the suitable range of $\alpha = 1 \ldots 2$, defined above in order to guarantee the total mass to be dominated by the high mass clumps and the total number of clumps by the low mass clumps, thus agrees with the full range of $\beta = E \ldots E+2$, guaranteeing the cloud image to be an *fBm* structure. For clumps with on average constant volume density, $\gamma = 3$, this is not the case. In this case, for mass spectra shallower than $\alpha = 1.666$ the structure has $\beta > 4$, i.e. a smooth projected image with a fractal dimension identical to the Euclidean dimension $E = 2$. At the steepest spectral index $\alpha = 2$ it only reaches $\beta = 3$, i.e. $H = 0.5$ or a fractal dimension of 2.5. It would reach the extreme value of $\beta = 2$ only at the extreme value $\alpha = 2.333$, i.e. for a structure whose mass is already dominated by the smallest clumps. The most likely case, $\gamma \approx 2.3$, is in between these two extremes.

The relation between power law mass spectral index α and fractal dimension d_H of the cloud, $\alpha = 3 - \frac{8-2d_H}{\gamma}$ is strictly valid for the assumed model of the cloud, i.e. an ensemble of clumps with a power law mass spectrum and a power law mass-size relation. We arrived at it by combining the relation between α and the *power spectrum* index β derived in Sect. 4, the relation between β and the drift index H derived in the Appendix, and the relation between H and the fractal dimension d_H defined as box coverage dimension of the $E + 1 = 3$-dimensional *fractional Brownian motion* surface, discussed in Sect. 3. Only the connection to the area-perimeter fractal dimension has not been derived explicitly but has been assumed to be valid following Voss (1988).

A different relation between the fractal dimension d_H of a molecular cloud and its clump mass spectral index α, namely $\alpha = 1 + \frac{d_H}{\gamma}$ in the notation adopted in the present paper, has been derived by Elmegreen & Falgarone (1996). This is clearly in conflict with the relation derived above. The discrepancy can be traced back to the different concepts used in deriving them and will be discussed together with the clumps size spectrum in the following subsection.

6.2. The clump size spectrum and the fractal dimension

A clump ensemble with power law mass spectrum $\frac{dN}{dM} \propto M^{-\alpha_M}$ and mass-size relation $M \propto L^\gamma$ has a size spectrum $\frac{dN}{dL} = \frac{dN}{dM}\frac{dM}{dL} \propto L^{\gamma(1-\alpha_M)-1}$; the index of the size spectrum, defined by $\frac{dN}{dL} \propto L^{-\alpha_L}$, is thus $\alpha_L = \gamma(\alpha_M - 1) + 1$ (this connection was actually already noted by Henriksen 1991). Inserting the relation between α and its fractal dimension from above, the size spectral index is $\alpha_L = 2\gamma + 2d_H - 7$.

In contrast, Mandelbrot states that the power law index of the clump size spectrum is given simply by the thus defined fractal dimension D, $\frac{dN}{dL} \propto L^{-(1+D)}$ (Mandelbrot 1983, page 118). This is clearly different from the above relation and the difference is due to the different concepts used. Mandelbrot derives this relation for *Koch-islands* generated the usual way via a generator that creates smaller islands in front of each island border line and counting the substructures thus generated. The number N of self-similar substructures on a scale λ greater than L then scales as $N(\lambda > L) \propto L^{-D}$.

The crucial point thus is, whether the $\frac{dN}{dL} \propto L^{-(1+D)}$ relation can be applied to fractal structures other than the *Koch-island* structures it has been derived for. We claim that this is not the case. The *fBm*-structure discussed above, generated as a clump ensemble with given mass spectrum and mass-size relation, gives a good counter example.

6.3. fBm-model versus Koch-island model structures

In this context it is important to note that a fractal structure with a given fractal dimension does not necessarily have a well defined size spectrum. Though this is clearly the case for the *Koch-island* structures analyzed by Mandelbrot and other hierarchically nested fractal structures, being generated by self similar replication of the basic structure at subsequently smaller scales, it is not the case in general. Again, the *fractional Brownian motion* structures give a good counter example: the fractal dimension is fixed once the *power spectrum* spectral index β is given. But an *fBm* structure as such has no size spectrum defined. The fact that the *power spectrum* has a certain amplitude at a given spatial frequency, i.e. that the image has a certain power on the corresponding length scale, still leaves open, whether this power is due to a few bright substructures of that size, or whether it is contributed by many weak substructures. The size distribution thus has to be specified separately, either directly or by a clump mass spectrum and a mass size relation, as was actually done with the ensemble of clumps which we showed to have *fractional Brownian motion* structure and a well defined fractal dimension.

In reverse, specifying a size spectrum of an ensemble of self similarly nested building blocks (such as the Gaussian clump ensemble discussed above) is not sufficient to fully characterize the fractal properties of its image. One needs, in addition, a link between the intensity resulting from a particular structure at its given size scale. In the case of the molecular cloud clump ensemble studied above, this is given by the mass-size relation for the clumps, $M \propto r^\gamma$, and the fact that the mass, resp. column density, determines the emitted intensity for an optically thin species [2].

Also, it is not at all obvious how to relate the hypothetical *Koch-island* structure, i.e. the set of boundary lines, for which the $\frac{dN}{dL} \propto L^{-(1+D)}$ relation has been derived, to a physical molecular cloud structure, i.e. a density or rather column density distribution. Elmegreen & Falgarone (1996) implicitly assume that the fractal dimension of the *Koch-island* structure is related to e.g. the fractal dimension defined via the area-perimeter relation of the iso-intensity contours of molecular clouds. The arguments given illustrate that this does not apply, at least for

[2] Simulations of molecular clouds with *fractional Brownian motion* density and velocity structures show that the shape of the *power spectrum* indeed depends on whether the molecular transition used as a tracer is assumed to be optically thick or thin (Ossenkopf et al., *in prep.*).

the *fBm*-structure generated as a clump ensemble with given mass spectrum and mass-size relation.

The important new idea in the Elmegreen & Falgarone (1996) paper is the suggestion that *the mass distribution in molecular clouds is the results of fractal gas structure*. They derive the relation $\alpha_M = 1 + \frac{D}{\gamma}$, which is essentially the basic connection between the mass spectral index α_M, size spectral index α_L and mass-size relation index γ as derived above, $\alpha_M = 1 + \frac{\alpha_L - 1}{\gamma}$, plus the additional assumption, that the size spectral index α_L is related to the fractal dimension D via the *Koch-island* relation $\alpha_L = 1 + D$. Our cloud structure analysis, based on a *fractional Brownian motion* cloud model, also shows that the mass distribution is determined by the fractal structure, and we derive a similar, but different, relation: $\alpha_M = 3 - \frac{8 - 2d_H}{\gamma}$.

It is, of course, of interest to check how well the observed values agree with either model. In this context, it is important to note, that the agreement between D/γ and α_M, both for the individual cloud surveys and for the ensemble distribution (Elmegreen & Falgarone 1996) cannot be taken to support the Koch-island model. This is, because D was actually not determined independently. It rather is derived from the size spectral index $\alpha_L = 1 + D$. The fact that the fitted values agree with the trivial $\alpha_M = 1 + \frac{\alpha_L - 1}{\gamma}$ relation simply confirms that the observed clump masses and sizes are derived in a consistent way. This is true both for the individual cloud data sets with their larger scatter of the particular values for α_L (respectively D in the context of that paper), γ, and α_M, as well as for the total ensemble of the data sets. It has nothing to do with the cloud structure or its fractal characteristics.

The close numerical agreement between the average value of $d_H = 2.35$ derived from the various fits to the clump size spectra by Elmegreen & Falgarone, and the range of values expected from fractal analysis via area-perimeter studies, giving $d = 1.3 - 1.5$ for the fractal dimension of the iso-intensity contours, and hence 2.3-2.5 for the fractal dimension of the 2-dimensional image, thus has to be regarded as coincidental. In fact, the detailed case study of the Polaris Flare presented in Sects. 2 and 4 shows that the area-perimeter fractal dimension in this case is $d = d_H - 1 = 1.6$, well consistent with the value of $\beta = 2.8$ derived independently, and hence also consistent with the relation $\alpha = 3 - \frac{8 - 2d_H}{\gamma}$ and the fitted values of $\alpha = 1.8$ and $\gamma = \frac{\beta}{3 - \alpha} = 2.3$. The size spectral index derived with the *fBm*-model, $\alpha_L = \gamma(\alpha_M - 1) + 1 = 2.84$, of course has to and does agrees with the value fitted to the observed size spectrum (Heithausen et al. 1998). In contrast, the relation $\alpha = 1 + \frac{d_H}{\gamma}$ (according to Elmegreen & Falgarone 1996) together with the measured values of α and β (and hence γ) for the Polaris Flare would result in $d_H = 1.8 < 2$, i.e. formally $d = d_H - 1 = 0.8$, even outside the range of allowed values ($d = 1$ to 2) for the area-perimeter fractal dimension of the contour lines.

Our analysis supports the Elmegreen & Falgarone (1996) result that the mass distribution of molecular clouds is closely connected to the fractal structure. Clearly, the different concepts used to describe the cloud structure result in different relations between the various indices involved. Based on the arguments presented in the preceding paragraphs, we prefer the *fBm*-structure concept to describe molecular clouds.

7. Discussion

7.1. Implications for the underlying 3-dimensional structure

The result from Sect. 5, namely that an ensemble of randomly positioned clumps with a given power law mass spectrum and a given mass-size relation has a *fractional Brownian motion* projected image, brings up the question whether the reverse conclusion can also be drawn: i.e. does the decomposition of an *fBm*-structure (power law *power spectrum* and random phases) into (Gaussian) clumps give the corresponding power law mass spectrum? Trying to answer this question clearly touches on two important issues: the first one concerns the connection between the underlying 3-dim structure corresponding to the observed 2-dim projection, the second one concerns the velocity structure related to the *fBm*-density distribution. It is obvious, that both issues are not independent: only the velocity structure in observed molecular cloud spectra allows the identification of individual clumps, which otherwise would merge into indistinguishable larger structures due to the overlap along the line of sight.

Nevertheless we can derive certain constraints for the 3-dim structure from the fact that the observed 2-dimensional projection has *fBm*-structure. The following always assumes that the observations are in an optically thin line, so that the observed image directly corresponds to the column density, i.e. the density structure integrated along the line of sight. From the fact that the projection of the 3-dimensional structure, i.e. the integration along the line of sight direction z, in Fourier space corresponds to taking the $k_z = 0$-cut of the 3-dimensional *Fourier transform*, we can infer that the 3-dimensional *Fourier transform* must be such, that its $k_z = 0$-cut has a power law *power spectrum* with the same spectral index as its 2-dimensional projection, i.e. the observed image. From the Copernican principle that the line of sight direction cannot be a preferred direction for the cloud structure, we can then conclude that the 3-dimensional cloud density structure must be such, that in Fourier space any 2-dimensional cut through its origin must give a power law *power spectrum*. This shows that the full 3-dimensional *power spectrum* also follows a power law, with the same spectral index as that of the 2-dimensional projected image. It does tell nothing, however, about the 3-dimensional phase distribution, although the assumption seems reasonable that they are as randomly distributed as the 2-dimensional phases. This is an ad hoc assumption, however, and one should keep in mind that the phases of the 3-dimensional Fourier image might well have some special correlation that is not visible in the 2-dimensional projection. One should remember that, as was discussed in Sect. 3, the reverse conclusion is always true: the $(E-1)$-dimensional projection of an E-dimensional structure with a power law *power spectrum* has again a power law *power spectrum* with the same spectral index.

Along this line of reasoning, the 3-dimensional structure thus also has a power law *power spectrum* whose spectral in-

dex is, according to the analysis of the observed 2-dimensional projection, close to 2.8. If the 3-dimensional phase distribution is in fact also completely random, this has very important consequences. It implies that the 3-dimensional structure is completely dominated by surface. A 3-dimensional *fBm* structure is limited to the range $\beta = 5 \ldots 3$, corresponding to $H = 0 \ldots 1$. The corresponding volume-surface relation for the fractal structure of the iso- density surface (the 3-dimensional analogon to the perimeter/area relation of the iso-intensity contours), then has a fractal dimension in the range $d_H = E+1-H = 3 \ldots 2$, i.e. $A \propto V^{d_H/3}$. At the minimum value of $H = 0$, i.e. $d_H = 3$, this already corresponds to the surface increasing proportional to the volume. The value of $\beta = 2.8$ for a 3-dim structure derived above, would nominally imply $H = (\beta - E)/2 = -0.1$, i.e. an even faster increase of surface with volume.

For a full understanding of the 3-dim cloud structure a link to the velocity structure is crucial. The velocity structure is important not only as a tool to tell overlapping 3-dim spatial structure apart, and to keep the emission of individual clumps from mutual shielding in the radiative transfer. Physically, the velocity structure must be linked to the density structure via the magneto-hydrodynamic equations describing the turbulent internal cloud motions. Ultimately, a proper description of this magneto hydrodynamic turbulence should describe the cloud structures observed. We are obviously far from reaching this goal. A simple approach, assuming independent *fBm*-distributions both for the density and the velocity structure, results in surprisingly realistic looking molecular cloud spectra which even satisfy some scaling relations such as the size-line width relation, $\Delta v \propto \Delta r^{0.5}$, over a limited range of scales. Future work will have to investigate these aspects in detail. Observationally we can get further constraints on the velocity structure e.g. by applying the Δ-*variance* analysis introduced above not only to the integrated intensity image of the molecular cloud, but also to individual velocity channel maps. These investigations will be presented in a future paper together with the Δ-*variance* analysis of a broader selection of observed molecular clouds (Bensch et al., *in prep.*).

7.2. Observational limits

The fact that detailed observations of molecular cloud structure, covering a significant dynamic range in spatial scales and also in the signal to noise ratio within a reasonable integration time, have become possible only within the last decade is linked to rapid progress in technology. The high sensitivity of large mm-wave telescopes and the excellent low noise performance of SIS-heterodyne receivers available at the low-J carbon monoxide line frequencies result in acceptable observing times of order several days for a decent size cloud mapping project. However, higher sensitivity receivers are not to be expected as the present day receivers already reach close to quantum limited performance; also, telescopes substantially larger than the IRAM 30m-telescope or the planned 50m LMT project are beyond technical feasibility. Mapping speed will profit from future array receiver systems. Extension of the structure analysis down to angular scales below the diffraction limit of the large single dish telescopes will only be possible with interferometric techniques.

It is thus of particular importance to estimate the observing time needed for extension of a cloud map to higher angular resolution with an interferometer array. Let us thus consider for simplicity and consistency the situation, where we want to observe a single resolution element of a large scale cloud map with higher angular resolution using an interferometer of antennas identical to the single dish used for the low angular resolution map. The effective system temperature (including receiver sensitivity, telescope efficiency and atmospheric losses) for each interferometer element and the single dish telescope are assumed to be identical. The noise level reachable in a given integration time and resolution bandwidth with the interferometer scales as (see Downes 1989)

$$\Delta T_{int} = \frac{L^2}{D^2\sqrt{N}} \Delta T_{sd},$$

where ΔT_{sd} is the noise achieved with the single dish telescope in the same given integration time, L is the length of the longest baseline, D is the diameter of each interferometer antenna, and $N = n(n-1)/2 \approx n^2/2$ is the number of baselines for a number n of interferometer elements. The resolution achieved with the interferometer scales as $\frac{\theta_{int}}{\theta_{sd}} = \frac{D}{L}$. The noise per resolution element then scales as

$$\Delta T_{int} = \left(\frac{\theta_{sd}}{\theta_{int}}\right)^2 \frac{1}{\sqrt{N}} \Delta T_{sd} \frac{\sqrt{t_{sd,pixel}}}{\sqrt{t_{int}}}.$$

The interferometer observes all $\left(\frac{\theta_{sd}}{\theta_{int}}\right)^2$ resolution elements within its field of view simultaneously. The single dish telescope has to observe each resolution element separately for a time $t_{sd,pixel}$. The scaled up single dish map with the same number of pixels as the interferometer map thus takes a total time $t_{sd} = \left(\frac{\theta_{sd}}{\theta_{int}}\right)^2 t_{sd,pixel}$. For the interferometer map to be a true scaled down version of the larger map, the signal to noise ratio per resolution element has to be the same as for the single dish map. The scaling of the signal level with resolution is given by the assumed *fractional Brownian motion* structure, which says that the structure in the signal at a scale θ scales $\propto \theta^H$ with $H = (\beta - 2)/2$ (see Sect. 3). The signal structure expected at both resolutions thus scales as

$$\Delta S_{int} = \left(\frac{\theta_{int}}{\theta_{sd}}\right)^{\beta/2-1} \Delta S_{sd}.$$

Combining the above relations and solving for equal signal to noise at the resolution of both maps gives the scaling of the total integration times:

$$t_{int} = \left(\frac{\theta_{sd}}{\theta_{int}}\right)^{\beta} \frac{1}{N}\, t_{sd}.$$

The same equation can be derived by considering the increase in integration time with higher resolution according to

$\left(\frac{\theta_1}{\theta_2}\right)^{(\beta-2)}$ due to the $\propto \theta^H$ decrease of the signal level for an otherwise identical, but larger single dish telescope; the reduced efficiency of an n-element interferometer of the same total size (and hence angular resolution) due to only a fraction $\epsilon = \frac{nD^2}{L^2} = n\left(\frac{\theta_1}{\theta_2}\right)^2$ of the aperture being filled, this efficiency entering squared into the ratio of integration times; and the spatial multiplexing advantage of the interferometer, $\left(\frac{\theta_1}{\theta_2}\right)^2$, observing all resolution elements within the field of view simultaneously. Combining these factors and using $n^2/2 \approx N$ reproduces the above relation.

We see that the total integration time rapidly increases with increasing resolution, $t \propto \theta^{-\beta}$. This increase is compensated by the decrease of integration time in proportion to the number of interferometer baselines. With the value of $\beta = 2.8$ derived above, and assuming a 5-element interferometer such as the IRAM Plateau-de-Bure instrument, i.e. $N = 10$, a submap of a single resolution element of the large scale single dish map with the interferometer at a 10 times higher resolution would thus take about 60 times as long as the total large scale map. This is unrealistically long to persue, considering the already very long observing times needed for decent size single dish maps with adequate signal to noise ratio. Extending studies of cloud structures to higher angular resolution will thus be feasible only with very large ($n \approx 30-60$) future interferometer arrays.

7.3. Beyond fractional Brownian motion structure

The present paper discusses molecular cloud structure in the framework of what is commonly called "monofractal structure". The actual cloud structure is certainly more complex and many different structures with the same mono-fractal characteristics are possible. A few recent papers have attempted to characterise observed clouds with multifractal methods. They show that the cloud structure indeed shows multifractal properties, both in the velocity distribution (Miesch & Bally 1994) and in the column density distribution (Chappell & Scalo 1997). However, they also seem to indicate that these multifractal properties vary from cloud to cloud. Whether this is due to the limited data base available and possible systematic errors in the analysis, or whether observed molecular clouds in fact fall into a single "universality class" is not clear at the moment. Molecular clouds clearly need more than one single parameter, e.g. a single fractal dimension, a single *power spectrum* spectral index, or a single power law index of their clump mass distribution, to fully characterise their structure. In the present paper, we explicitely excluded multifractal aspects from the present discussion and rather concentrate on a comparison of and the possibility to unify the various monofractal measures of cloud structure obtained with the different methods commonly used.

8. Summary

We have introduced a new method, the Δ-*variance* analysis, to study the structure of molecular cloud images. The drift behavior, measured by the Δ-*variance*, is linked to the shape of the *power spectrum* of the cloud image. Application to the observed CO-maps of the Polaris Flare and the subset of the FCRAO outer galaxy survey shows, that at least for these two examples, the *power spectrum* has power law shape and the power law index is close to $\beta = 2.8$ in both cases. Analysis of the phase distribution of the images shows them to be completely random. The application of these concepts to a more complete sample of observed cloud images will be studied in a future paper (Bensch et al., *in prep.*).

We have shown that other parameters derived via independent ways to measure and characterize fractal cloud structure, such as the traditional area-perimeter relation, are related to the drift behavior measured via the Δ-*variance* method, or the power law index of the *power spectrum*. This also includes other, at first sight independent, properties such as the mass spectral index derived from clump decomposition of observed cloud images. We have shown that an ensemble of randomly positioned clumps with a given power law index of the clump mass spectrum and a given power law mass-size relation has a *fractional Brownian motion* structure of its projected image. The clump mass spectral index of molecular clouds, derived by clump decomposition of the observed intensity and velocity distribution, thus, together with the derived index of the mass-size relation, determines the power law index of the image *power spectrum*, $\beta = (3-\alpha)\gamma$. The observed values for the mass spectral index α and the mass-size index γ of the Polaris Flare, both derived from a clump decomposition of the observed cloud image over a large range of spatial scales, as well as the power law index of the *power spectrum*, β, independently derived via the Δ-*variance* analysis agree with each other along this relation.

These results show that, similar to the result by Elmegreen & Falgarone (1996), the mass spectrum of molecular cloud clumps is closely linked to the fractal structure of the gas. The relation between clump mass and clump size spectrum and the fractal dimension of the cloud image derived within the *fBm* concept agrees with the observed values, but is in conflict with their relation based on the *Koch-island* model for the fractal structure.

The above results suggest that the basic characteristics of molecular cloud structure might well be described in a unified way as a *fractional Brownian motion* structure, characterized by a single parameter, e.g. the power law index of the *power spectrum*. We show that images synthesized along these rules as *fractional Brownian motion* images indeed look very much like observed molecular cloud maps. Such synthesis thus provides a potentially very useful tool to generate artificial structures well representing real molecular clouds, e.g. for radiative transfer modeling (Ossenkopf et al., *in prep.*). Also, hydrodynamic modeling of molecular clouds has to meet the structural characteristics of such *fBm*-structures.

One should not forget, however, that molecular cloud structure is likely to be much more complex than the simple concept of *fractional Brownian motion*, which nevertheless applies well to the basic characteristics of observed, 2-dimensional projected cloud images. The clouds themselves are 3-dimensional and it might well be that the 3-dimensional structure is much more

complex than a simple *fBm* structure, which only emerges in projection. Also, the turbulent velocity fields within molecular clouds (providing pseudo 3-dimensional information from molecular line maps which only makes such analysis as clump decomposition methods possible) are an important ingredient and have to be included into a full treatment and understanding of molecular cloud structure. Nevertheless, the characteristics derived for the 2-dimensional projected images already give certain constraints on the 3-dimensional structure. If the 3-dimensional phases are essentially as randomly distributed as is the case for the phases of the 2-dimension image, the measured power law index of the 2-dimensional image implies that the surface grows proportional to volume for the 3-dim cloud structure, and that hence most of the material is surface material. This is in accordance with the well established fact that even ^{12}CO, though being a completely optically thick tracer, measures cloud mass, as well as the recently emerging view, that most line emission from molecular cloud tracers is largely dominated by surface effects.

Examining the applicability of the concepts presented to a larger sample of observed molecular images is certainly one important goal of future work. Another one will be, to extend the observations to much larger spatial coverage and higher signal to noise. The discussion shows that, due to the steep power law decrease observed in the *power spectrum* of cloud images, this will be very difficult observationally even with large focal plane single dish arrays and large size future interferometers.

Acknowledgements. The authors thank B. Elmegreen, B. Deiss, R. Schieder, Y.-Z. Yue for many helpful comments and clarifying discussions on the manuscript. This research was supported by the Deutsche Forschungsgemeinschaft through grant SFB 301C.

Appendix A: statistical properties of 1-dimensional random functions: average, variance, autocorrelation function, power spectrum, Allan-variance and Δ-variance

We shortly summarize the definitions and basic relations between the quantities commonly used to describe the statistical properties of random, or noise, functions. We closely follow the notion used in standard textbooks on the topic, e.g. Davenport & Root (1987) or Bracewell (1986). We also introduce a new quantity, the Δ-*variance*, which turns out to be very useful in characterizing the drift behavior and *power spectrum* also in higher dimensions.

We consider a 1-dimensional, real valued function $s(t)$, e.g. a time series, like the output voltage of a detector device, that varies randomly but has a well defined average, variance and other statistical properties. Its average over a time interval T centered at time t is $\bar{s}(t,T) = \frac{1}{T}\int_{t-\frac{T}{2}}^{t+\frac{T}{2}} s(t')\,dt'$. Its mean value is then

$$\bar{s} = \langle s(t)\rangle = \lim_{T\to\infty} \bar{s}(t,T),$$

and is assumed to be independent of t. To be more precise, the time average $\bar{s}$ equals the statistical average $\langle s(t)\rangle$ provided that $s(t)$ is a stationary random function with a finite time-correlation scale. In the following we assume $\bar{s} = 0$. This is no essential restriction as any random function with non zero average can be changed into one with zero average by subtracting the constant average value, $s'(t) = s(t) - \bar{s}$ with $\bar{s}' = 0$. The *autocorrelation function* is defined as $A_s(\tau) = \langle s(t)s(t+\tau)\rangle$ and the variance is $\sigma_s^2 = \langle (s(t)-\bar{s})^2\rangle = \langle s^2(t)\rangle = A_s(\tau{=}0)$.

The *Fourier transform* of $s(t)$ is defined as $\tilde{s}(f) = \int_{-\infty}^{+\infty} s(t)\exp(-2\pi i f t)\,dt$. Due to $s(t)$ being real valued, the *Fourier transform* is hermitian: $\tilde{s}(-f) = \tilde{s}^*(f)$. For the *convolution* of two functions $g(x)$ and $h(x)$, we use the notation $\{g(...) * h(...)\}(x) = \int_{-\infty}^{+\infty} g(x')\,h(x-x')\,dx'$. Though somewhat more cumbersome than the common notation $g(x) * h(x)$, it avoids inconsistencies inherent in the latter. These arise from the fact that

$$\{g(...) * h(...)\}(ax) = a\ \{g(a...) * h(a...)\}(x),$$

whereas the common notation suggests the incorrect result $g * h(ax) = g(ax) * h(ax)$.

The above definition of the *Fourier transform* is not fully sufficient as it is not clear that the integral exists. In order to ensure convergence of the Fourier integrals of random functions, one rather defines a truncated function $s_T(t) = s(t)\cdot\sqcap(\frac{t}{T})$, using the *rectangle function* $\sqcap(x) = \begin{cases} 1, & |x| \le 1/2 \\ 0, & |x| > 1/2 \end{cases}$. It approaches $s(t)$ in the limit of infinite T. Its *Fourier transform* is

$$\begin{aligned}\tilde{s}_T(f) &= \int_{-\infty}^{+\infty} s_T(t)\exp(-2\pi i f t)\,dt \\ &= \{\tilde{s}(...) * T\,\mathrm{sinc}(T\,...)\}(f),\end{aligned}$$

where the last equality is due to the convolution theorem and uses the fact that the *Fourier transform* of $\sqcap(t)$ is the *sinc*-function, $\mathrm{sinc}(x) = \frac{\sin(\pi x)}{\pi x}$. It is, of course, only valid if the *Fourier transform* $\tilde{s}(f)$ exists. The *Fourier transform* of the random function $s(t)$ can then be defined "in the limit" (Bracewell 1986) as

$$\begin{aligned}\tilde{s}(f) &= \lim_{T\to\infty}\tilde{s}_T(f) = \left\{\tilde{s}(...) * \lim_{T\to\infty}[T\,\mathrm{sinc}(T\,...)]\right\}(f) \\ &= \{\tilde{s}(...) * \delta(...)\}(f).\end{aligned}$$

The second equality again assumes that the *Fourier transform* $\tilde{s}(f)$ exists. The last equality uses the fact that $T\mathrm{sinc}(fT)$ approaches the *impulse function* $\delta(f)$ in the limit of infinite T; this relation confirms the consistency of the notation in case the *Fourier transform* exists.

We can now define the *normalized autocorrelation function*

$$\begin{aligned}a_{s_T}(\tau) &= \frac{\int_{-\infty}^{+\infty} s_T(t)s_T(t+\tau)\,dt}{\int_{-\infty}^{+\infty} s_T^2(t)\,dt} \\ &= \frac{\frac{1}{T}\int_{-\infty}^{+\infty} s_T(t)s_T(t+\tau)\,dt}{\frac{1}{T}\int_{-\infty}^{+\infty} s_T^2(t)\,dt}.\end{aligned}$$

The denominator approaches the variance σ^2 in the limit of infinite T, the nominator approaches the *autocorrelation function* $A(\tau)$. Thus,

$$a_s(\tau) = \lim_{T\to\infty} a_{s_T}(\tau) = \frac{1}{\sigma^2} A_s(\tau).$$

Due to $s(t)$ being real valued, using the convolution theorem and *Rayleigh's theorem*,

$$\int_{-\infty}^{+\infty} |s_T(t)|^2\, dt = \int_{-\infty}^{+\infty} |\tilde{s}_T(f)|^2\, df,$$

the *Fourier transform* of the *normalized autocorrelation function* of s_T is

$$\tilde{a}_{s_T}(f) = \frac{|\tilde{s}_T(f)|^2}{\int_{-\infty}^{+\infty} |\tilde{s}_T(f)|^2\, df},$$

so that we can define the *power spectrum* $P_s(f)$ as the *Fourier transform* of the *autocorrelation function*

$$P_s(f) \;=\; \tilde{A}_s(f) = \sigma^2 \lim_{T\to\infty} \tilde{a}_{s_T}(f) = \lim_{T\to\infty} \frac{1}{T} |\tilde{s}_T(f)|^2.$$

As $s(t)$ is real valued, the *power spectrum* is an even function, $P(-f) = P(f)$. It is common practice to define, instead of $P(f)$, the *power spectrum* $\mathcal{P}(f)$ for positive frequencies only, and to fold the power at negative frequencies into the positive frequency domain:

$$\mathcal{P}(f) = P(f) + P(-f) = 2P(f), f \geq 0.$$

We can then write the *autocorrelation function* as

$$A(\tau) = \int_{-\infty}^{+\infty} P(f) \exp(2\pi i f\tau)\, df = \int_0^{\infty} \mathcal{P}(f) \cos(2\pi f\tau)\, df,$$

and its back transform

$$\mathcal{P}(f) = 4 \int_0^{\infty} A(\tau) \cos(2\pi f\tau)\, d\tau.$$

For the variance we get $\sigma^2 = A(\tau{=}0) = \int_0^{\infty} \mathcal{P}(f)\, df$.

In order to describe the drift behavior of the random function $s(t)$ one often uses the *two point correlation function*

$$\begin{aligned} G_s(\tau) \;&=\; \langle (s(t+\tau) - s(t))^2 \rangle \\ &=\; 2(\langle s^2(t) \rangle - \langle s(t) s(t+\tau) \rangle) \\ &=\; 2\left[\sigma^2 - A_s(\tau)\right] = 2\sigma^2 \left[1 - a_s(\tau)\right]. \end{aligned}$$

Another useful quantity, now commonly called *Allan variance*, was introduced by Allan (1966) in order to characterize the drift behavior. It is the variance of the difference between subsequent averages over a time interval T. With the average over time T as defined above, which we also can write as the convolution with the appropriately scaled *rectangle function*,

$$\bar{s}(t,T) = \frac{1}{T} \int_{t-\frac{T}{2}}^{t+\frac{T}{2}} s(t')\, dt' = \left\{ s(...) * \frac{1}{T} \sqcap\!(\frac{...}{T}) \right\}(t),$$

we can write for the difference between subsequent averages

$$\begin{aligned} d(t,T) \;&=\; \bar{s}(t-\tfrac{T}{2},T) - \bar{s}(t+\tfrac{T}{2},T) \\ &=\; -\left\{ \bar{s}(...,T) * \frac{2}{T} \top\!\!\!\perp(\frac{...}{T}) \right\}(t) \\ &=\; -\left\{ s(...) * \frac{2}{T} \sqcup\!\!\sqcap(\frac{...}{T}) \right\}(t), \end{aligned}$$

where $\top\!\!\!\perp(x) = \frac{1}{2}\left[\delta(x-\frac{1}{2}) - \delta(x+\frac{1}{2})\right]$ is the notation for the *odd impulse pair* function, and we introduced the notation

$$\sqcup\!\!\sqcap(x) = \left\{ \sqcap(...) * \top\!\!\!\perp(...) \right\}(x) = \begin{cases} -1/2, & -1 \leq x < 0 \\ +1/2, & 0 < x \leq 1 \\ 0, & \text{elsewhere} \end{cases}$$

for the *down-up-rectangle* function. The *Allan variance* is the variance of these differences: $\sigma_A^2(T) = \frac{1}{2}\langle d^2(t,T)\rangle_t$, where the factor $\frac{1}{2}$ is introduced to match the original definition. In the time domain $\sigma_A^2(T)$ can be calculated from the *autocorrelation function* $a(t)$ (Barnes et al. 1971; Schieder, *in prep.*), i.e.

$$\sigma_A^2(T) = \frac{\sigma^2}{T} \int_{-T}^{+T} (T - |t|)\, \left[a(t) - a(t+T)\right]\, dt.$$

In the Fourier domain it can be expressed as

$$\begin{aligned} \sigma_A^2(T) \;&=\; \frac{1}{2} A_{d(...,T)}(\tau{=}0) = \frac{1}{2} \int_0^{\infty} \mathcal{P}_{d(...,T)}(f)\, df \\ &=\; 2 \int_0^{\infty} \mathcal{P}_s(f)\, \frac{\sin^4(\pi f T)}{(\pi f T)^2}\, df, \end{aligned}$$

where we have used the fact that the *power spectrum* of the convoluted function $d(t,T)$ is the product of the *power spectra* of the functions being convoluted, and the *Fourier transform* of $\frac{1}{T}\sqcap(\frac{t}{T})$ is $\frac{\sin(\pi f T)}{(\pi f T)}$, the *Fourier transform* of $\frac{2}{T}\top\!\!\!\perp(\frac{t}{T})$ is $(2/i)\, \sin(\pi f T)$.

The statistical properties of the random function $s(t)$, such as variance and *Allan variance*, are thus completely determined by its *power spectrum*, or the *Fourier transform* thereof, its *autocorrelation function*. The *Allan variance* in particular is the filtered average of the *power spectrum*, the filter function being $2\frac{\sin^4(\pi f T)}{(\pi f T)^2}$. This filter function has successive maxima at the roots of the algebraic equation $\tan(x) = 2x$, with $x = \pi f T$. The first peak, at $f = 1.166/(\pi T) \approx 1/(\pi T)$ is the highest with a peak value of 1.05 , independent of T. The width of this peak is $\propto 1/T$. Further peaks at higher frequencies are damped $\propto 1/f^2$. Using *Rayleigh's theorem*, its integral can be seen to give $2\int_0^{\infty} \frac{\sin^4(\pi f T)}{(\pi f T)^2} d\, f \;=\; \frac{1}{2T}$. The filter function, including the additional factor $2T$, thus gives another representation of the δ-function in the limit of large T,

$$\lim_{T\to\infty} 2T \frac{\sin^4(\pi f T)}{(\pi f T)^2} = \delta(f).$$

In the same sense, the *autocorrelation function* can be regarded as the filtered average of the *power spectrum* with a filter function $\cos(2\pi f\tau)$.

As this paper largely deals with random functions with a power law *power spectrum* we now summarize the results for this special case. For a 1-dimensional random function (e.g. a time series) with a power law *power spectrum*, $\mathcal{P}(f) \propto f^{-\beta}, \beta \geq 0$ over a range of frequencies $f_l < f < f_h$ between a properly defined low and high frequency cutoff as defined in Appendix C, an analytic expression has been derived both for the *autocorrelation function* and the *Allan variance* for times $\frac{1}{2\pi f_h} \ll t \ll \frac{1}{2\pi f_l}$ (Barnes et al. 1971; Schieder, *in prep.*). We only quote their result here and refer to the original papers and our more extensive discussion, including also 2- and 3-dimensional random functions, in Appendix C for the details. Note that $\beta = 0$ is the well known case of purely white noise, $\beta = 1$ is so called *flicker noise*, $\beta = 2$ corresponds to the well studied *random walk*. For the *normalized autocorrelation function* one obtains

$$a(\tau) = \left\{ \begin{array}{ll} 1 - \frac{1}{6}\frac{\beta-1}{\beta-3}\,(2\pi f_l\tau)^2, & 3<\beta, \\ 1 - \frac{1}{3}(\frac{11}{6} - \gamma + \ln\frac{1}{2\pi f_l \tau})\,(2\pi f_l\tau)^2, & \beta=3, \\ 1 - \frac{1}{\Gamma(\beta+1)\,\mathrm{sinc}(\frac{\beta-1}{2})}\,(2\pi f_l\tau)^{\beta-1}, & 1<\beta<3, \end{array} \right\} \tau \ll \frac{1}{2\pi f_l}$$

$$\left\{ \begin{array}{ll} \frac{1}{\ln(f_h/f_l)}\,(1 - \gamma + \ln\frac{1}{2\pi f_l \tau}), & \beta=1, \\ \pi/2\,\Gamma(2-\beta)\,\mathrm{sinc}(\frac{\beta}{2})\,(2\pi f_h\tau)^{-(1-\beta)}, & 0<\beta<1, \end{array} \right\} \begin{array}{l} \frac{1}{2\pi f_h} \ll \\ \tau \ll \frac{1}{2\pi f_l} \end{array}$$

$$\left\{ \begin{array}{ll} \mathrm{sinc}(2 f_h \tau), & \beta=0, \end{array} \right\} \text{ all } \tau$$

where $\gamma = 0.577\ldots$ is *Euler's constant*. Thus, $a(\tau)$ decreases from its value of unity at $\tau = 0$ in a power law fashion $\propto \tau^{\beta-1}$ for $0 < \beta \leq 3$. For the range $0 < \beta \leq 1$ this power law behavior only holds for sufficiently large values of $\tau \gg 1/(2\pi f_h)$ and with an additional logarithmic term at $\beta = 1$ and $\beta = 3$ (see also Appendix C). For larger values of β, i.e. $\beta > 3$, $a(\tau)$ drops $\propto -\tau^2$ independent of β. Note that the high frequency cutoff matters only for $0 < \beta \leq 1$. For $\beta = 0$ and very large high frequency cutoff the sinc-function approaches the δ-function and we get the well known result for white noise $a(\tau) = \frac{1}{2 f_h}\,\delta(\tau), \beta = 0$.

The *two point correlation function*

$$G(\tau) = 2\sigma^2\,[1 - a(\tau)]$$

correspondingly shows a power law behavior for small τ only as long as $\beta > 1$. For $1 < \beta < 3$, one gets $G(\tau) \propto \tau^{\beta-1}$, turning over into $G(\tau) \propto \tau^2$ at $\beta = 3$.

A similar expression gives the *Allan variance*

$$\sigma_A^2(T)/\sigma^2 = \left\{ \begin{array}{ll} \frac{\beta-1}{\beta-3}\,(2\pi f_l T)^2, & 3<\beta, \\ \frac{1}{3}(\frac{29}{12} - \gamma + \ln\frac{2^{4/3}}{2\pi f_l T})\,(2\pi f_l T)^2, & \beta=3, \\ \frac{2^{\beta+1}-4}{\Gamma(\beta+2)\,\beta\,\mathrm{sinc}(\frac{\beta-1}{2})}\,(2\pi f_l T)^{\beta-1}, & 1<\beta<3, \end{array} \right\} T \ll \frac{1}{2\pi f_l}$$

$$\left\{ \begin{array}{ll} \frac{2\,\ln(2)}{\ln(f_h/f_l)}, & \beta=1, \\ \frac{4-2^{\beta+1}}{\Gamma(\beta+2)\,\beta\,\mathrm{sinc}(\frac{\beta-1}{2})}\,(2\pi f_h T)^{-(1-\beta)}, & 0<\beta<1, \end{array} \right\} \begin{array}{l} \frac{1}{2\pi f_h} \ll \\ T \ll \frac{1}{2\pi f_l} \end{array}$$

$$\left\{ \begin{array}{ll} (2 f_h T)^{-1}, & \beta=0, \end{array} \right\} \frac{1}{2\pi f_h} \ll T$$

The behavior of the *Allan variance* is thus very similar to that of the *two point correlation function*, varying as $T^{\beta-1}$ for $0 < \beta \leq 3$,and as T^2 for $\beta > 3$. However, due to the fact that the integral over the filter function $2\frac{\sin^4(\pi f T)}{(\pi f T)^2}$ exists and is finite, the *Allan variance* has a regular behavior for $\beta = 0$ even for large f_h, whereas the *autocorrelation function* has a δ-function irregularity. Similarly, the logarithmic divergence for $\beta = 1$ has been removed due to the filter function starting $\propto f^2$ for small f (see Appendix C).

Note that the validity of the expression above is limited to $T \ll 1/(2\pi f_l)$ for $\beta \neq 0$. For very large integration time T the *Allan variance* always drops $\propto T^{-1}$, i.e. like in the case of white noise, $\beta = 0$, independent of the spectral index of the *power spectrum*, and in fact independent on the shape of the *power spectrum* in general, as long as the *power spectrum* approaches a finite positive value in the low frequency limit, $\mathcal{P}(0+) > 0$. This behavior results because of the δ-function like behavior of the filter function in the limit of large T, so that

$$\begin{aligned} \sigma_A^2(T) &= \frac{2}{2T}\int_0^{+\infty} \mathcal{P}(f)\,2T\frac{\sin^4(\pi f T)}{(\pi f T)^2}\,df \\ &\approx \frac{1}{2T}\int_{-\infty}^{+\infty} \mathcal{P}(f)\,\delta(f)\,df = \frac{\mathcal{P}(0)}{2T} \end{aligned}$$

(more precisely, $\mathcal{P}(0)$ above should be replaced by its limiting value $\mathcal{P}(0+) > 0$). For a difference measurement with very long integration time T the noise level reached is thus always larger than the white noise value $\sigma^2/(2 f_h T)$, as can be seen from the fact that $\sigma^2 = A(\tau{=}0) = \int_0^\infty \mathcal{P}(f)\,df \leq \mathcal{P}(0)\,f_h$ as long as $\mathcal{P}(0) \geq \mathcal{P}(f)$ and $\mathcal{P}(f) = 0, f > f_h$. These conditions are met with the *power spectrum* and its cutoffs as defined in Appendix C.

The definition of the *Allan variance* via the average difference $d(t,T)$ as above is, of course, ad hoc. Other definitions are possible and equally adequate. One could, for example, use a "before and after" difference, respectively *double difference*,

$$\begin{aligned} \Delta(t,T) &= \bar{s}(t,T) - \frac{1}{2}\,[\bar{s}(t-T,T) + \bar{s}(t+T,T)] \\ &= \left\{ s(...) * \frac{1}{T}\sqcap\!\sqcup\!\sqcap(\frac{\cdots}{T}) \right\}(t), \end{aligned}$$

where we have introduced the *down-up-down rectangle* function

$$\begin{aligned} \sqcap\!\sqcup\!\sqcap(x) &= \left\{ \begin{array}{ll} 1, & |x| \leq 1/2 \\ -1/2, & 1/2 < |x| \leq 3/2 \\ 0, & \text{elsewhere} \end{array} \right. \\ &= \sqcap(x + \frac{1}{2}) - \sqcap(x - \frac{1}{2}) = -2\left\{ \sqcap * \top^{\perp} \right\}(x) \\ &= -2\left\{ \sqcap * \top^{\perp} * \top^{\perp} \right\}(x) \end{aligned}$$

for the convolving function. From its definition it is obvious that the *power spectrum* of $\sqcap\!\sqcup\!\sqcap(t)$ is $4\frac{\sin^6(\pi f)}{(\pi f)^2}$. We define the Δ-*variance* in analogy to the *Allan variance* as the variance of this double difference, i.e. $\sigma_\Delta^2(T) = \frac{1}{2}\langle\Delta^2(t,T)\rangle_t$. Expressed via the *power spectrum* it is then obviously given by

$$\sigma_\Delta^2(T) = 2\int_0^\infty \mathcal{P}_s(f)\,\frac{\sin^6(\pi f T)}{(\pi f T)^2}\,df.$$

For a power law *power spectrum* $\mathcal{P}(f) \propto f^{-\beta}$ one obtains (see Appendix C)

$$\sigma^2_\Delta(T)/\sigma^2 = \left\{ \begin{array}{lll} c_{>4}(2\pi f_l T)^4, & 5<\beta, & \\ c_4(c'_4+\ln\frac{1}{2\pi f_l T})\,(2\pi f_l T)^4, & \beta=5, & \Big\} \; T \ll \frac{1}{2\pi f_l} \\ c_{1,5}(2\pi f_l T)^{\beta-1}, & 1<\beta<5, & \\ c_1, & \beta=1, & \Big\} \; \frac{1}{2\pi f_h} \ll \\ c_{<1}(2\pi f_h T)^{-(1-\beta)}, & 0<\beta<1, & \Big\} \; T \ll \frac{1}{2\pi f_l} \\ \frac{3}{8}(f_h T)^{-1}, & \beta=0, & \Big\} \; \frac{1}{2\pi f_h} \ll T \end{array} \right.$$

where the c_i can be determined by comparison with the highest order terms in the corresponding expression for $X(\tau)$ in Appendix C. Note that the Δ-*variance* has no special behavior at $\beta = 3$, in contrast to the standard *Allan variance*. It rather shows a logarithmic divergence and turns over into a β-independent power law slope, T^4, at $\beta \geq 5$. As explained in Appendix C, this is due to the fact that the *double difference* filter function starts $\propto f^4$ for small f.

The *down-up-down rectangle* function can also be written as the difference of a *rectangle function* with width T and a 3 times wider negative *rectangle function*:

$$\frac{1}{T}\sqcup\!\!\sqcap\!\!\sqcup(\frac{t}{T}) = \frac{3}{2}\left[\frac{1}{T}\sqcap(\frac{t}{T}) - \frac{1}{3T}\sqcap(\frac{t}{3T})\right].$$

This form readily lends itself to further generalization and can easily be extended to define the Δ-*variance* also in higher dimensions (see Appendix B). There is no need to define the average with equal weighting, as we have done above. Of particular interest might be a Gaussian weighting function, $G(x) = \exp(-\pi x^2)$, thus defining the average as

$$\bar{s}_G(t,T) = \left\{ s(...) * \frac{1}{T} G(\frac{\cdots}{T}) \right\}(t).$$

The corresponding *Gaussian down-up-down* function, replacing the *down-up-down rectangle* function, is then

$$\frac{1}{T}\bigcup\!\!\bigcap\!\!\bigcup(\frac{t}{T}) = \frac{3}{2}\left[\frac{1}{T}G(\frac{t}{T}) - \frac{1}{3T}G(\frac{t}{3T})\right],$$

and the *Gaussian weighted average double difference* can be written as

$$\Delta_G(t,T) = \left\{ s(...) * \frac{1}{T}\bigcup\!\!\bigcap\!\!\bigcup(\frac{\cdots}{T}) \right\}(t).$$

As the Gaussian weighting function is its own *Fourier transform*, the *Fourier transform* of $\frac{1}{T}\bigcup\!\!\bigcap\!\!\bigcup(\frac{t}{T})$ is $\frac{3}{2}\left[\exp(-\pi f^2 T^2) - \exp(-9\pi f^2 T^2)\right]$. The variance of the *Gaussian weighted average double difference*, i.e. the *Gaussian* Δ-*variance*, is then given by

$$\sigma^2_{\Delta_G}(T) = \frac{1}{2}\int_0^\infty \mathcal{P}_s(f)\,\frac{9}{4}\left(e^{-\pi f^2 T^2} - e^{-9\pi f^2 T^2}\right)^2 df.$$

According to the results of Appendix C it has, for a power law power spectrum, the same behavior with delay time T as the Δ-*variance* $\sigma^2_\Delta(T)$.

Appendix B: the definition of the Δ-*variance* as the analogue of the *Allan Variance* in higher dimensions

The definition of the *variance of the double difference* as given in the preceding appendix can be straightforwardly extended to higher dimension. Before we do so, we shortly repeat the definition of the statistical properties of random functions, such as *power spectrum* and *autocorrelation function* in higher dimensions.

Consider a scalar function $s(\boldsymbol{r})$ in E-dimensional space. Its average over an E-dimensional sphere with diameter D, centered at $\boldsymbol{r}$, is defined as the convolution with the *normalized E-dimensional ball function*, i.e.

$$\bar{s}(\boldsymbol{r}, D) = \left\{ s(...) * \frac{1}{\mathcal{V}_E\,(\frac{D}{2})^E}\sqcap(\frac{|...|}{D}) \right\}(\boldsymbol{r}),$$

where $\mathcal{V}_E = \frac{2\,\pi^{\frac{E}{2}}}{E\,\Gamma(\frac{E}{2})}$ is the volume of the E-dimensional unit sphere. Note that this definition is fully consistent with the definition for the 1-dimensional case given in Appendix A. Its mean value

$$\bar{s} = \langle s(\boldsymbol{r})\rangle = \lim_{D\to\infty} \bar{s}(\boldsymbol{r}, D)$$

is assumed to be independent of $\boldsymbol{r}$ (homogeneity) and is assumed to vanish: $\bar{s} = 0$. The *autocorrelation function* and *variance* are defined in analogy to the 1-dimensional case: $A_s(\boldsymbol{\rho}) = \langle s(\boldsymbol{r}) s(\boldsymbol{r}+\boldsymbol{\rho})\rangle$, $\sigma_s^2 = \langle s^2(\boldsymbol{r})\rangle = A_s(\boldsymbol{\rho}=0)$.

The E-dimensional *Fourier transform* is

$$\tilde{s}(\boldsymbol{f}) = \int_{\boldsymbol{r}} s(\boldsymbol{r})\exp(-2\pi i \boldsymbol{f}\cdot\boldsymbol{r})\,d^E\boldsymbol{r},$$

the corresponding back transform

$$s(\boldsymbol{r}) = \int_{\boldsymbol{f}} \tilde{s}(\boldsymbol{f})\exp(+2\pi i \boldsymbol{f}\cdot\boldsymbol{r})\,d^E\boldsymbol{f}.$$

As $s(\boldsymbol{r})$ is real valued, $\tilde{s}(\boldsymbol{f})$ is hermitian: $\tilde{s}(-\boldsymbol{f}) = \tilde{s}^*(\boldsymbol{f})$.

To ensure convergence of the Fourier integrals for a random function, we define the truncated function $s_D(\boldsymbol{r}) = s(\boldsymbol{r})\cdot\sqcap(\frac{|\boldsymbol{r}|}{D})$. In complete analogy to the 1-dimensional case we can then define the *Fourier transform*, the *normalized autocorrelation function* and the *power spectrum* in the limit of $D\to\infty$. In particular, we get

$$P_s(\boldsymbol{f}) = \tilde{A}_s(\boldsymbol{f}) = \lim_{D\to\infty}\frac{1}{\mathcal{V}_E\,(\frac{D}{2})^E}|\tilde{s}_D(\boldsymbol{f})|^2.$$

Due to $s(\boldsymbol{r})$ being real valued, $P(\boldsymbol{f})$ is even.

If we assume in addition, that the statistical properties of $s(\boldsymbol{r})$ are isotropic, the *autocorrelation function* will depend on the magnitude of $\boldsymbol{\rho}$ only, i.e. $A(\boldsymbol{\rho}) = A(|\boldsymbol{\rho}|)$. The *power spectrum*, as its *Fourier transform*, is then also only dependent on $|\boldsymbol{f}|$, as the angular dependence in the $\exp(-2\pi i \boldsymbol{f}\cdot\boldsymbol{r}) = \exp(-2\pi i f r\cos\theta)$-term can be integrated out. The relation between the two radial functions is then given by (Bracewell 1986, p. 254)

$$A(\rho) = \mathcal{S}_E\int_0^\infty P(f)\,\frac{\Gamma(\frac{E}{2})\,J_{\frac{E}{2}-1}(2\pi f\rho)}{(\pi f\rho)^{\frac{E}{2}-1}}f^{E-1}\,df$$

and the identical back transform obtained by exchanging $A(\rho)$ with $P(f)$ and ρ with f. Here, $\mathcal{S}_E = \frac{2\,\pi^{\frac{E}{2}}}{\Gamma(\frac{E}{2})} = E\,\mathcal{V}_E$ is the surface of the unit sphere in E dimensions. The kernel in the integral, $\Gamma(\frac{E}{2})\,J_{\frac{E}{2}-1}(2\pi f\rho)/(\pi f\rho)^{\frac{E}{2}-1}\,f^{E-1}$ reduces to $\cos(2\pi f\rho)$ in the 1-dimensional case. In 2 dimensions it is $J_0(2\pi f\rho)\,f$, giving the *Hankel transform*; in 3 dimensions it is $\sin(2\pi f\rho)/(2\pi f\rho)$. We can now define the analogue to $\mathcal{P}(f)$ in the E-dimensional case, by incorporating the E-dimensional solid angle into the definition of the *power spectrum*: $\mathcal{P}(f) = \mathcal{S}_E\,P(f)$,so that

$$A(\rho) = \int_0^\infty \mathcal{P}(f)\,\frac{\Gamma(\frac{E}{2})\,J_{\frac{E}{2}-1}(2\pi f\rho)}{(\pi f\rho)^{\frac{E}{2}-1}} f^{E-1}\,df.$$

The back transform then reads

$$\mathcal{P}(f) = {\mathcal{S}_E}^2 \int_0^\infty A(\rho)\,\frac{\Gamma(\frac{E}{2})\,J_{\frac{E}{2}-1}(2\pi f\rho)}{(\pi f\rho)^{\frac{E}{2}-1}}\rho^{E-1}\,d\rho.$$

Before we proceed, we will shortly discuss some properties of the *normalized E-dimensional ball function* and its *Fourier transform*. Straightforward algebra, using the fact that $x^\nu\,J_{\nu-1}(x) = \frac{d}{dx}\,[x^\nu\,J_\nu(x)]$, gives for the *Fourier transform* of the *normalized E-dimensional ball function*

$$\text{F.T. of } \frac{1}{\mathcal{V}_E\,(\frac{D}{2})^E}\Pi(\frac{r}{D}) = \frac{\Gamma(\frac{E}{2}+1)\,J_{\frac{E}{2}}(\pi f D)}{(\pi f D/2)^{\frac{E}{2}}}.$$

In the limit of $D\to\infty$, $\Pi(\frac{r}{D})$ is constant and equals unity everywhere. Its *Fourier transform* is the E-dimensional δ-function. We thus obtain the useful result

$$\lim_{D\to\infty}\mathcal{V}_E(\frac{D}{2})^E\frac{\Gamma(\frac{E}{2}+1)\,J_{\frac{E}{2}}(\pi f D)}{(\pi f D/2)^{\frac{E}{2}}} = {}^E\delta(\boldsymbol{f}).$$

For a power law *power spectrum*, $\mathcal{P}(f)\propto f^{-\beta}, \beta\geq 0, f_l < f < f_h$, we derive in Appendix C the following behavior of the *normalized autocorrelation function*:

$$a(\rho) = \begin{cases} 1-c_{>E+2}(2\pi f_l\rho)^2, & E+2<\beta, \\ 1-c_{E+2}(c'_{E+2}+\ln\frac{1}{2\pi f_l\rho})\,(2\pi f_l\rho)^2, & \beta=E+2, \\ 1-c_{E,E+2}(2\pi f_l\rho)^{\beta-E}, & E<\beta<E+2, \end{cases} \rho\ll\frac{1}{2\pi f_l}$$

$$\begin{cases} c_E(c'_E+\ln\frac{1}{2\pi f_l\rho}), & \beta=E, \\ c_{<E}(2\pi f_h\rho)^{-(E-\beta)}, & 0<\beta<E, \end{cases} \frac{1}{2\pi f_h}\ll\rho\ll\frac{1}{2\pi f_l}$$

$$\frac{\Gamma(\frac{E}{2}+1)\,J_{\frac{E}{2}}(2\pi f_h\rho)}{(\pi f_h\rho)^{\frac{E}{2}}}, \quad \beta=0, \quad \text{all } \rho$$

In analogy to the 1-dimensional case discussed in Appendix A, $a(\rho)$ thus drops from its value of unity at $\rho = 0$ in a power law fashion, i.e. $\propto\rho^{\beta-E}$, as long as $\beta < E+2$. For the range of $0<\beta\leq E$ this is only true once ρ gets sufficiently large, i.e. ($\ll\frac{1}{2\pi f_h}$). For $\beta = E$, it is thus approximately independent of ρ, except for the additional logarithmic term also present at $\beta = E+2$. For $\beta > E+2$ it turns over into an decrease $\propto -\rho^2$, i.e. a β-independent behaviour. For $\beta = 0$, we obtain, similar to the 1-dimensional case, in the limit of large f_h

$$\lim_{f_h\to\infty} a(\rho) = \frac{1}{\mathcal{V}_E\,f_h^E}\,{}^E\delta(\boldsymbol{\rho}), \text{for } \beta = 0.$$

Correspondingly, the E-dimensional *two point correlation function* $G(\rho) = 2\sigma^2\,[1-a(\rho)]$ increases in a power law fashion for small ρ only as long as $\beta > E$. In the range $E<\beta<E+2$ we have $G(\rho)\propto\rho^{\beta-E}$, turning over into a β-independent behavior $G(\rho)\propto\rho^2$ for $\beta > E+2$, with an additional logarithmic term at $\beta = E+2$. Note that the simple dimensional argument given in Voss (1988), pp. 91-92, to derive the relation between the *power spectrum* power law index and the drift behavior power law index does give neither the turnover to the $\propto\rho^2$-behavior for $\beta > E+2$ nor the logarithmic divergences at $\beta = E$ and $\beta = E+2$.

We can now define the E-dimensional *down-up-down ball function* as the analogue to the *down-up-down rectangle function* used in the 1-dimensional case (note that *down-up-down* describes the variation along the diameter of the spherically symmetric function):

$$\overset{E}{\sqcup\!\sqcap\!\sqcup}(r) = \frac{3^E}{(3^E-1)}\left[\Pi(r) - \frac{1}{3^E}\Pi(\frac{r}{3})\right] = \begin{cases} 1, & r\leq 1/2 \\ -1/(3^E-1), & 1/2<r\leq 3/2 \\ 0, & \text{elsewhere} \end{cases}.$$

With the abbreviation $\bigodot_{D,E}(r) = \frac{1}{\mathcal{V}_E\,(\frac{D}{2})^E}\,\overset{E}{\sqcup\!\sqcap\!\sqcup}\,(\frac{r}{D})$, the E-dimensional *difference of averages at average distance* D is then obtained by convolution of $s(\boldsymbol{r})$ and $\bigodot_{D,E}(r)$:

$$\Delta(r,D,E) = \left\{ s(...) * \underset{D,E}{\bigodot}(|...|) \right\}(\boldsymbol{r}),$$

which is the analogue to the 1-dimensional *double difference* defined in Appendix A, $\Delta(t,T) = \Delta(t,T,1)$.

The corresponding analogue of the Δ-*variance* in E dimensions is then

$$\sigma^2_{\Delta,E}(D) = \frac{1}{\mathcal{S}_E}A_{\Delta(r,D,E)}(\rho{=}0) = \int_0^\infty P(f)\,|\underset{D,E}{\tilde{\bigodot}}(f)|^2\,f^{E-1}\,df,$$

where we have introduced the factor $\frac{1}{\mathcal{S}_E}$ as the E-dimensional generalization of the historical factor $\frac{1}{2}$ in the 1-dim *Allan variance*.

With the *Fourier transform* of the *normalized E-dimensional ball function* given above, the filter function in the Δ-*variance* can be written as

$$|\underset{D,E}{\tilde{\bigodot}}(f)|^2 = \left(\frac{3^E\,\Gamma(\frac{E}{2}+1)}{3^E-1}\right)^2\left[\frac{J_{\frac{E}{2}}(\pi f D)}{(\pi f D/2)^{\frac{E}{2}}} - \frac{J_{\frac{E}{2}}(3\pi f D)}{(3\pi f D/2)^{\frac{E}{2}}}\right]^2.$$

Series expansion of the *Bessel*-functions shows that the filter function starts $\propto f^4$ at small f. As in the 1-dimensional case, it has a first peak at $f\approx 1/(\pi D)$, which narrows down in

width as D grows larger. *Rayleigh's theorem* shows that its E-dimensional integral

$$\mathcal{S}_E \int_0^\infty |\tilde{\bigodot}_{D,E}(f)|^2 \, f^{E-1} \, df = \frac{3^E}{(3^E-1)\,\mathcal{V}_E(\frac{D}{2})^E}.$$

For large D, the filter function thus approaches

$$\frac{3^E}{3^E-1}\frac{1}{\mathcal{V}_E\,(\frac{D}{2})^E}\,{}^E\delta(\boldsymbol{f}).$$

As in the 1-dimensional case, this implies that for large D the Δ-*variance* goes as

$$\sigma^2_{\Delta,E}(D) = \frac{3^E}{\mathcal{S}_E\,(3^E-1)}\,\frac{P(0)}{\mathcal{V}_E\,(\frac{D}{2})^E},$$

similar to the white noise behavior (see below).

For a power law *power spectrum*, $P(f) \propto f^{-\beta}, \beta \geq 0, f_l < f < f_h$, one obtains (see Appendix C)

$$\sigma^2_{\Delta,E}(D)/\sigma^2 =$$

$$\left\{\begin{array}{lll}
c_{>E+4}(2\pi f_l D)^4, & E+4<\beta, & \left.\begin{array}{l}\\ \\ \\ \end{array}\right\} \; D \ll \frac{1}{2\pi f_l} \\
c_{E+4}(c'_{E+4}+\ln\frac{1}{2\pi f_l D})\,(2\pi f_l D)^4, & \beta=E+4, & \\
c_{E,E+4}(2\pi f_l D)^{\beta-E}, & E<\beta<E+4, & \\
c_E & \beta=E, & \left.\begin{array}{l}\\ \\ \end{array}\right\} \; \frac{1}{2\pi f_h} \ll \\
c_{<E}(2\pi f_h D)^{-(E-\beta)}, & 0<\beta\leq E, & \quad D \ll \frac{1}{2\pi f_l} \\
\frac{3^E}{\mathcal{S}_E\,(3^E-1)}\frac{1}{\mathcal{V}_E{}^2}(f_h D/2)^{-E}, & \beta=0, & \left.\begin{array}{l}\\ \\ \end{array}\right\} \; \frac{1}{2\pi f_h} \ll D
\end{array}\right.$$

Note that the Δ-*variance* varies as $D^{\beta-E}$ for the full range of $0 \leq \beta \leq E+4$. It shows a logarithmic divergence and turns over into a β-independent power law slope, T^4, at $\beta = E+4$. As explained in Appendix C, this is due to the fact that the corresponding filter function starts $\propto f^4$ for small f.

For white noise, $P(f) = \left\{\begin{array}{ll} P(0), & f \leq f_h \\ 0, & f > f_h \end{array}\right.$, the Δ-*variance* drops inversely proportional to the averaging volume, i.e. $\propto \mathcal{V}_E\,(D/2)^{-E}$, consistent with Gaussian statistics. The factor in front corresponds to the volume average squared weights of the inner ball and the outer shell, and the ad hoc factor $\frac{1}{\mathcal{S}_E}$. Comparison with the general behavior for large D (see above) shows that the Δ-*variance* at large drift scales, although it drops $\propto D^{-E}$ as in the white noise case, is always larger than the white noise value; this is due to the fact that $\sigma^2 = A(\rho = 0) = \int_{\boldsymbol{f}} P(f) d^E\boldsymbol{f} \leq P(0)\,\mathcal{V}_E f_h^E$ as long as $P(0) \geq P(f)$ and $P(f) = 0, f > f_h$.

Appendix C: relation between the power law index of the power spectrum and the drift behavior

In this Appendix we will derive the general connection between the power law index of the *power spectrum* and the drift behavior, as e.g. given by the *autocorrelation function*, the *Allan variance* for 1-dimensional time series, or in general for the Δ-*variance* of an E-dimensional random function whose statistical properties are isotropic and homogeneous, i.e. spherically symmetric. As shown in Appendix A and B, these statistical quantities are in general defined as integrals over the *power spectrum* weighted with some scaled filter function $w(\tau f)$. We thus consider in the general, E-dimensional case a quantity

$$X(\tau) = \mathcal{S}_E \int_0^\infty P(f)\, w(\tau f)\, f^{E-1}\, df.$$

As the filter function is the squared modulus of the *Fourier transform* of the corresponding convolving function in the spatial domain, defining the appropriate differences of averages characterizing the statistical quantity $X(\tau)$ under question, we know that $w(u)$ is even, $w(u) = w(-u)$. Its series expansion for small frequencies thus contains only even power law terms. Moreover, as the convolving function in the spatial domain is square integrable, the same is true for its *Fourier transform*, so that the integral $\int_0^\infty w(u)\, f^{E-1}\, df$ exists.

Only in the special case of the *autocorrelation function*, where the expression for the E-dimensional *Fourier transform* gives for the filter function

$$w(u) = \Gamma(\frac{E}{2})\, J_{\frac{E}{2}-1}(2\pi u)/(\pi u)^{(\frac{E}{2}-1)},$$

the situation is slightly more subtle, and will be discussed separately below.

We now assume a power law *power spectrum*, i.e. $P(f) \propto f^{-\beta}, \beta \geq 0$. This shape cannot be valid for all f. At low frequencies, we have to introduce a cutoff f_l where $P(f)$ turns over towards a constant, finite value $P(0)$. The requirement of a finite value $P(0)$ is, due to the *Fourier transform* relation between the *power spectrum* and the *autocorrelation function* mathematically equivalent to the requirement that $\int_0^\infty a(\tau)\, dt$ exists, i.e. is finite. This is always the case if $a(\tau)$ drops faster than $1/\tau$ for large τ. We also assume that $P(f) = 0$ for all frequencies higher than the high frequency cutoff f_h. The high frequency cutoff ensures, for a power law index shallower than $\beta = E$, a finite total "energy", respectively a finite *variance*, i.e. guarantees that $\sigma^2 = \mathcal{S}_E \int_0^\infty P(f) f^{E-1} df$ exists and is finite. It is irrelevant for a steeper *power spectrum*.

Similar to the definition used by Schieder *in prep.*, we thus assume a *power spectrum*

$$P(f) = P_0 \left\{\begin{array}{ll} 1, & f<f_l \\ \frac{f^{-\beta}-f_h^{-\beta}}{f_l^{-\beta}-f_h^{-\beta}}, & f_l \leq f < f_h \\ 0, & f_h \leq f \end{array}\right.$$

This definition formally includes the case $\beta = 0$ if we additionally set $f_l = f_h$ for $\beta = 0$. With the normalization condition $\sigma^2 = \mathcal{S}_E \int_0^\infty P(f) f^{E-1} df$, a straightforward calculation shows that

$$P_0 = \sigma^2 \left\{\begin{array}{ll} \frac{1}{\mathcal{V}_E\, f_h^E}, & \beta=0 \\ \frac{1}{\mathcal{V}_E\, f_l^E}\,\frac{1}{E}\,\frac{1-(f_l/f_h)^E}{\ln(f_h/f_l)}, & \beta=E \\ \frac{1}{\mathcal{V}_E\, f_l^E}\,\frac{\beta-E}{\beta}\,\frac{1-(f_l/f_h)^\beta}{1-(f_l/f_h)^{\beta-E}}, & \beta\neq 0,E \end{array}\right. .$$

We can then calculate the expression for $X(\tau)$ and obtain, after rearranging terms appropriately

$$X(\tau)/\sigma^2 = \kappa_\beta \begin{cases} \left[\frac{W_{E-1}(\tau f_l)-W_{E-1}(0)}{(\tau f_l)^E} - \left(\frac{f_h}{f_l}\right)^{E-\beta} \frac{W_{E-1}(\tau f_h)-W_{E-1}(0)}{(\tau f_h)^E} + \frac{W_{E-\beta-1}(\tau f_h)-W_{E-\beta-1}(\tau f_l)}{(\tau f_l)^{E-\beta}}\right], & \beta\neq 0 \\ \frac{W_{E-1}(\tau f_h)-W_{E-1}(0)}{(\tau f_h)^E}, & \beta=0 \end{cases},$$

where

$$\kappa_\beta = \begin{cases} E, & \beta=0 \\ \frac{1}{\ln(f_h/f_l)}, & \beta=E \\ \frac{E(\beta-E)}{\beta}\ \frac{1}{1-(f_h/f_l)^{E-\beta}}, & \beta\neq 0,E \end{cases}.$$

Here we have introduced the abbreviation

$$W_a(z) = \int_1^z w(x)\, x^a\, dx.$$

Due to the properties of the filter function $w(x)$ discussed above, these integrals exist and have finite values for any finite value of z.

We now consider the limit of a large high frequency cutoff and a small low frequency cutoff, i.e. $f_l \ll f_h$. We can then write

$$\kappa_\beta \approx \begin{cases} E, & \beta=0 \\ \frac{E(E-\beta)}{\beta}\left(\frac{f_l}{f_h}\right)^{E-\beta}, & \beta<E \\ \frac{1}{\ln(f_h/f_l)}, & \beta=E \\ \frac{E(\beta-E)}{\beta}, & \beta>E \end{cases}.$$

Only certain terms survive in leading order in the expression for $X(\tau)$:

$$X(\tau)/\sigma^2 \begin{cases} = E\frac{W_{E-1}(\tau f_h)-W_{E-1}(0)}{(\tau f_h)^E}, & \beta=0 \\ \approx \frac{E(E-\beta)}{\beta}\left[-\frac{W_{E-1}(\tau f_h)-W_{E-1}(0)}{(\tau f_h)^E} + \frac{W_{E-\beta-1}(\tau f_h)-W_{E-\beta-1}(\tau f_l)}{(\tau f_h)^{E-\beta}}\right], & 0<\beta<E \\ = \frac{1}{\ln(\frac{f_h}{f_l})}\left[W_{-1}(u) - \frac{W_{E-1}(u)-W_{E-1}(0)}{u^E}\right]\Big|_{u=\tau f_l}^{\tau f_h}, & \beta=E \\ \approx \frac{E(\beta-E)}{\beta}\left[\frac{W_{E-1}(\tau f_l)-W_{E-1}(0)}{(\tau f_l)^E} + \frac{W_{E-\beta-1}(\tau f_h)-W_{E-\beta-1}(\tau f_l)}{(\tau f_l)^{E-\beta}}\right], & \beta>E \end{cases}.$$

Considering now values of τ well in between the low and high frequency cutoff, i.e. $1/f_h \ll \tau \ll 1/f_l$, we have to worry about the behavior of $W_{E-\beta-1}(z)$ for large and small z. As discussed above, $W_{E-1}(z)$ approaches a finite value for large z: $W_{E-1}(z) \approx W_{E-1}(\infty) + \mathcal{O}(\frac{1}{z}), z\to\infty$. The same is true for $W_{E-\beta-1}(z), \beta>0$ as the additional factor $x^{-\beta}$ in the integrand can only improve the convergence of the already integrable function $w(x)\, x^{E-1}$ at large x.

Only in the special case that $X(\tau)$ is the autocorrelation function, i.e. $w(u) = \Gamma(\frac{E}{2})\, J_{\frac{E}{2}-1}(2\pi u)/(\pi u)^{\frac{E}{2}-1}$, the behavior at large z is different. The integral can be evaluate analytically and gives

$$E\frac{W_{E-1}(\tau f_h) - W_{E-1}(0)}{(\tau f_h)^E} = \frac{\Gamma(\frac{E}{2}+1)\, J_{\frac{E}{2}}(2\pi\tau f_h)}{(\pi\tau f_h)^{\frac{E}{2}}} \overset{f_h\to\infty}{=} \frac{1}{\mathcal{V}_E\, f_h^E}\ {}^E\delta(\boldsymbol{\tau}).$$

In this special case, $[W_{E-1}(z) - W_{E-1}(0)]/z^E$ thus does not approach a definite value for large z, but keeps oscillating with decreasing amplitude. In the 1-dimensional case, this is exactly the sinc-function with its corresponding behavior, approaching the δ-function in the limit of large high frequency cutoff.

At the low frequency cutoff, $\tau f_l \ll 1$, we can use the series expansion of $w(u) = \sum_{k=0}^\infty w_{2k}\, u^{2k}$ to obtain

$$W_{E-\beta-1}(\epsilon) = \begin{cases} -\sum_{k=0}^\infty w_{2k}\frac{1-\epsilon^{2k+E-\beta}}{2k+E-\beta}, & \beta\neq E+2m,\ m=0,1,... \\ \sum_{k=0,\neq m}^\infty w_{2k}\frac{1-\epsilon^{2(k-m)}}{2(k-m)} + w_{2m}\,\ln(\frac{1}{\epsilon}), & \beta=E+2m,\ m=0,1,... \end{cases}.$$

With $w_{2n},\ n\geq 1$ being the first non zero coefficient in the series expansion of $w(x)$, i.e. $w_{2m}=0,\ 1<m<n;\ w_{2n}\neq 0$, we then get to leading order in τ

$$X(\tau)/\sigma^2 \begin{cases} = E\big[W_{E-1}(\infty) + \sum_{k=n}^\infty \frac{w_{2k}}{E+2k}\big]\frac{1}{(\tau f_h)^E}, & \begin{cases}\beta=0 \\ \frac{1}{f_h}\ll\tau\end{cases} \\ \approx \frac{E(E-\beta)}{\beta}\big[W_{E-\beta-1}(\infty) + \sum_{k=n}^\infty \frac{w_{2k}}{E+2k-\beta}\big]\frac{1}{(\tau f_h)^{(E-\beta)}}, & \begin{cases}0<\beta<E \\ \frac{1}{f_h}\ll\tau\ll\frac{1}{f_l}\end{cases} \\ \approx \frac{1}{\ln(\frac{f_h}{f_l})}\big[W_{-1}(\infty) + \sum_{k=n}^\infty \frac{w_{2k}}{2k} + w_0(\frac{1}{E}+\ln\frac{1}{\tau f_l})\big], & \begin{cases}\beta=E \\ \frac{1}{f_h}\ll\tau\ll\frac{1}{f_l}\end{cases} \\ \approx w_0 + \frac{E(\beta-E)}{\beta}\big[W_{E-\beta-1}(\infty) + \sum_{k=n}^\infty \frac{w_{2k}}{E+2k-\beta}\big](\tau f_l)^{\beta-E}, & \begin{cases}E<\beta<E+2n \\ \tau\ll\frac{1}{f_l}\end{cases} \\ \approx w_0 + \frac{2n\,E}{E+2n}\big[W_{-(2n+1)}(\infty) + \sum_{k=n+1}^\infty \frac{w_{2k}}{2(k-n)} + w_{2n}(\frac{1}{E+2n}+\ln\frac{1}{\tau f_l})\big](\tau f_l)^{2n}, & \begin{cases}\beta=E+2n, \\ \tau\ll\frac{1}{f_l}\end{cases} \\ \approx w_0 + w_{2n}\frac{E(\beta-E)}{(E+2n)(\beta-E-2n)}(\tau f_l)^{2n}, & \begin{cases}E+2n<\beta \\ \tau\ll\frac{1}{f_l}\end{cases} \end{cases}.$$

Thus, $X(\tau)/\sigma$ basically goes $\propto \tau^{(\beta-E)}$ for $\beta \leq E+2n$, and turns over into $\propto \tau^{2n}$ behavior for larger values of β.

In detail, one notes that for $\beta > E$ only the low frequency cutoff is relevant, i.e. the expressions stay valid for $f_h \to \infty$, independent of τ. For $\beta = E$, $X(\tau)$ shows a logarithmic divergence for small τ unless $w_0 = 0$. It always shows a logarithmic divergence for small τ when $\beta = E+2n$, i.e. at the turnover from the $\propto \tau^{\beta-E}$–behavior of $X(\tau)$ for $\beta < E+2n$ to the $\propto \tau^{2n}$–behavior at $\beta > E+2n$.

From this general expression we can derive the special cases given in Appendix A and B. Let us consider as an example the 1-dimensional *autocorrelation function*. With $E = 1$ and $w(u) = \cos(2\pi u)$ we have $w_0 = 1$, $w_2 = -2\pi^2$, i.e. $n = 1$ in the above definition. As the reader can verify, this immediately leads to the approximation for $\beta > 3$ as given in Appendix A. The integrals $W_\beta(z)$ can in this case be calculated in closed form:

$$
\begin{aligned}
&W_{-\beta}(z) \\
&= \frac{1}{(2\pi)^{1-\beta}} \int_{2\pi}^{2\pi z} x^{-\beta} \cos x \, dx \\
&= \frac{1}{(2\pi)^{1-\beta}} \, \Re \left[\int_{2\pi}^{2\pi z} x^{-\beta} \exp(ix) \, dx \right] \\
&= \begin{cases} \frac{1}{1-\beta} \, \Re \left[u^{1-\beta} M(1-\beta, 2-\beta, 2\pi i u) \right] \Big|_{u=1}^{u=z}, & \beta \neq 2m+1 \\ \Re \left[-u^{-2m} \, E_{2m+1}(-2\pi i u) \right] \Big|_{u=1}^{u=z} & \beta = 2m+1 \end{cases},
\end{aligned}
$$

where $M(a,b,u)$ is a *Confluent Hypergeometric Function* (Kummer's Function), and $E_n(u)$ is the *nth-order Exponential Integral* (see Abramovitz & Stegun 1972). The expression in Appendix A then results from the asymptotic form of $M(1-\beta, 2-\beta, 2\pi i u)$ and $E_{2m+1}(2\pi i u)$ for large u, and their series expansions for $u = 1$ after a straightforward, but tedious calculation. The calculation for the standard *Allan variance* or for the *1-dimensional Δ-variance* proceeds very similar. This is also the case for the corresponding 3-dimensional expressions. In the 2-dimensional case, the corresponding integrals involving *integer order Bessel functions* do not allow a straightforward manipulation into a closed form.

References

Abramovitz M., Stegun, I.A., 1972, "Handbook of Mathematical Functions", Dover, New York.

Allan D.W., 1966, Proc. IEEE, Vol.54, No.2, 221.

Barnes J.A., Chi A.R., Cutler L.S., et al., 1971, IEEE Trans. IM, Vol.20, No.2, 105.

Bazell D., Desert F.X., 1988, ApJ 333, 353.

Bertoldi F., McKee C.F., 1996, *Self regulated star formation*. In: Chiao R.Y. (ed.) *Amazing Light*. Springer:NewYork, p. 41.

Bracewell R.N., 1986, The Fourier Transform and Its Applications, McGraw-Hill.

Castets A., Duvert J.E., Dutrey A. et al., 1990, A&A 234, 469.

Chappell D.W., Scalo, J., 1997, ApJ submitted.

Davenport W.B., Root W.L., 1987, An Introduction to the Theory of Random Signals and Noise, IEEE press, New York.

Dickman R.L., Kleiner S.C., 1985, ApJ 295, 479.

Dickman R.L., Horvath M.A., Margulis M., 1990, ApJ 365, 586.

Downes D., 1989, *Radio Astronomy Techniques*. In: Appenzeller I., Habing H.J., Lena P. (eds.) *Evolution of Galaxies, Astronomical Observations*. Springer Verlag:Heidelberg.

Elmegreen B.G., Falgarone E., 1996, ApJ 471, 816.

Falgarone E., Phillips T.G., 1996, ApJ 472, 191.

Falgarone E., Phillips T.G., Walker C., 1991, ApJ 378, 186.

Falgarone E., Panis J.-F., Heithausen A. et al., 1998, A&A 331, 669.

Gierens K., Stutzki J., Winnewisser G., 1991, A&A 259, 271.

Green D.A., 1993, MNRAS 262, 327.

Heithausen A., Thaddeus P., 1990, ApJ 353, L49.

Heithausen A., Bensch F., Stutzki J., Falgarone E., Panis J.F., 1998, A&A Letters 331, L65.

Henriksen R.N., 1991, ApJ 377, 500.

Heyer M., Brunt Ch., Howe, J. et al., 1997, FCRAO newsletter, vol. 8, p. 6.

Ho P.T.P., Townes, C.H., 1983, ARA&A 21, 239.

Houlahan M.P., Scalo J., 1992, ApJ 393, 172.

Howe J.E., Jaffe D.T., Genzel R., Stacey G.J., 1991, ApJ 373, 158.

Kleiner S.C., Dickman R.L., 1987, ApJ 312, 837.

Köster B., Störzer H., Stutzki J., Sternberg A., 1994, A&A 284, 545.

Kramer, C., Stutzki, J., Röhrig, R., and Corneliussen, U., 1998, A&A 329, 249.

Langer W.D., Wilson R.W., Anderson C.H., 1993, ApJ 408, L45.

Langer W.D., Velusamy T., Kuiper T.B.H. et al., 1995, ApJ 453, 293.

Larson R., 1992, MNRAS 256, 641.

Mandelbrot B.B., 1983, The Fractal Geometry of Nature, Freeman, San Francisco.

Martin H.M., Sanders D.B., Hills R.E., 1984, MNRAS 208, 35.

Miesch M.S., Bally J., 1994, ApJ 429, 645.

Peitgen H.O., Saupe D., 1988, The Science of Fractal Images, Springer, New York.

Perault M., Falgarone E., Puget J.L., 1986, A&A 157, 139.

Scalo J.M., 1990, In: Capuzzo-Doletta R. et al. (eds.), *Physical Processes in Fragmentation and Star Formation*. Reidel:Dordrecht, p. 151.

Schieder R., Tolls V., Winnewisser G., 1989, Experimental Astronomy, Vol.1, 1.

Snell R.L., Mundy L.G., Goldsmith P.F., Evans N.J., Erickson N.R., 1984, ApJ 276, 625.

Störzer H., Stutzki J., Sternberg A., 1996, A&A 310, 592.

Störzer H., Stutzki J., Sternberg A., 1997, A&A submitted.

Stutzki, J., 1993, *The Small Scale Structure of Molecular Clouds*. In: Klare G. (ed.) *Reviews of Modern Astronomy*, Vol. 6, Astronomische Gesellschaft, pp.209-231.

Stutzki J., Güsten R., 1990, ApJ 356, 513.

Stutzki J., Stacey G.J., Genzel R. et al., 1988, ApJ 332, 279.

Tauber J.A., 1996, A&A 315, 591.

Tauber J.A., Goldsmith P.F., Dickman R.L., 1991, ApJ 375, 635.

Vogelaar M.G.R., Wakker B.P., 1994, A&A 291, 557.

Voss R., 1988, *Fractals in Nature: from Characterization to Simulation*. In: Peitgen H.O., D.Saupe D. (eds.) *The Science of Fractal Images*. Springer:New York.

Williams J.P., De Geus E.J., Blitz L., 1994, ApJ 428, 693.

Zimmermann T., 1993, PhD Thesis, University of Cologne.

Zimmermann T., Stutzki J., 1993, Physica A 191, 79.

Zinnecker H., 1989, *Towards a theory in star formation*. In: Beckman J. (ed.) *Evolutionary phenomena in galaxies*. Cambridge University Press:Cambridge.